Original Article

A multi-objective optimisation approach for activity excitation of waste glass mortar

Junbo Sun [a], Yunchao Tang [b,c], Jianqun Wang [d], Xiangyu Wang [e,*], Jiaqing Wang [f], Zimei Yu [g], Qian Cheng [h], Yufei Wang [e,**]

[a] Institute for Smart City of Chongqing University in Liyang, Chongqing University, Jiangsu, 213300, China
[b] Key Laboratory of Disaster Prevention and Structural Safety of Ministry of Education, School of Civil Engineering and Architecture, Guangxi University, Nanning, 530004, China
[c] Guangxi Key Laboratory of Disaster Prevention and Engineering Safety, School of Civil Engineering and Architecture, Guangxi University, Nanning, 530004, China
[d] Hunan Provincial Key Laboratory of Structures for Wind Resistance and Vibration Control, School of Civil Engineering, Hunan University of Science and Technology, Xiangtan, 411201, China
[e] School of Design and Built Environment, Curtin University, Perth, WA, 6102, Australia
[f] College of Civil Engineering, Nanjing Forestry University, Jiangsu, 210037, PR China
[g] School of Engineering, The University of Western Australia, Perth, WA, 6009, Australia
[h] School of Civil Engineering, Chongqing University, Chongqing, 400030, China

ARTICLE INFO

ABSTRACT

Waste glass is promising to be recycled and reused in construction for sustainability. Silicon dioxide is the main component of glass, however, its pozzolanic activity is latent mainly due to its stable silica tetrahedron structure. To excite the activation of waste glass, chemical activation and mechanical grinding of waste glass powder (WGP) were investigated. As the supplementary, hydrothermal and combined (mechanical-chemical-hydrothermal) treatments were conducted on part of the WGP samples. The unconfined compression strength (UCS), expansion caused by alkali—silica reaction (ASR), and the microstructural morphology of WGP were investigated. The results showed the dosage threshold (around 2%) of the chemical activators (alkali and sodium sulfate) and the combined activation were optimal. Besides, a firefly algorithm (FA) based multi-objective optimisation model (MOFA) was applied to seek the Pareto fronts based on three objectives: UCS, ASR expansion, and Cost of mixture proportion. The objective functions of UCS and expansion were established through training the machine learning (ML) models where FA was used to tune the hyperparameters. The cost was calculated by a polynomial function. The ultimate values of root mean square error (RMSE) and correlation coefficient (R) showed the robustness of the ML models. Moreover, the Pareto fronts for mortars containing 300 μm and 75 μm WGPs were successfully obtained, which contributed to the practical application of waste glass in mortar production. In addition, the sensitivity

analysis was conducted to rank the importance of input variables. The results showed that curing time, activator's content, and WGP particle size were three essential parameters.

1. Introduction

Concrete is an essential component in architectural construction and civil engineering. However, the production process of concrete inevitably generates enormous carbon dioxide, exacerbating global warming. Therefore, it is imperative to ascertain novel supplementary cementitious materials [1—5]. Glass products are broadly utilised in daily life owing to their extensive sources, prominent plasticity, and durability so that the quantity of waste glass (WG) is increasing correspondingly. Improper disposal of waste glass occupies lands, wastes energy, and damages the ecological environment [6,7]. With sustainable development and green building becoming deeply appreciated, research on the WG application in concrete has received widespread attention [6,8,9]. The waste glass contains a large proportion of silica, which yields latent pozzolanic characteristics. Accordingly, partial replacement of cementitious materials with waste glass is a promising solution for waste glass reusing [10—12].

Research on concrete incorporating waste glass has gradually developed since the 1960s. However, Waste glass concrete is susceptible to alkali—silica reaction (ASR), resulting in local expansion and cracking of concrete which seriously affects the structure safety and limits its wide application [13,14]. Besides, waste glass cement cullet used as aggregate generally possesses lower workability and compressive strength than natural sand. This is because the crushed waste glass is often flat and elongated, restricting the shape and size of the aggregate. Previous studies reported that reducing the particle size of waste glass can effectively reduce the ASR expansion and improve mechanical performance, which was optimal at particle diameters ranging from 36 to 100 μm [15,16]. When the glass particles are ground to below 100 μm, its pozzolanic characteristic is greatly improved, which is superior even to fly ash [14,15,17]. Besides, the combination of waste glass with pozzolans (fly ash, silica fume, metakaolin, etc.) and lithium compounds also can alleviate the detrimental expansion [18—20]. Apart from the above methods, chemical and hydrothermal activations are also included, while the investigation on WG is challenging because of the complexity of the chemical activators' category and the temperature/pressure of the hydrothermal process [21,22].

Apart from ASR expansion and mechanical performance, the radiation shielding property of concrete containing waste glass is also a promising research objective which can be deeply explored in the future. It has been investigated on concrete containing different proportions of marble [23]. Regarding glass system, Al-Buriahi et al. [24] explored the radiation shielding property of $TeO_2 - Ag_2O - WO_3$ glass and stated that the contents of Ag_2O and WO_3 were essential parameters to influence the shielding property. The $TeO_2 - Na_2O - TiO$ glass system was also studied through PHITS Monte Carlo code, which was verified as an advanced shielding material for nuclear application [25]. Singh et al. [26] fabricated a novel bioactive glass system to possess desirable qualities for radiation shielding. The optical properties of bismuth incorporated chalcogenide glasses were also investigated accompanied by the structural shield property [27].

Regarding mortar mix design, the conventional method is a trial-and-error process based on numerous experimental data, which is time-consuming and labor-intensive. Moreover, it is error-prone to find optimal mixing ratios for multivariate experiments by summarising regularities and phenomena. The selection of the appropriate regression equation is complicated requiring skill and experience. It could lead to inaccurate outcomes if an explicit mathematical regression equation is implemented through the empirical model. Therefore, traditional methods fail to meet the requirements of modeling complex nonlinear behavior and uncertainty. Therefore, the artificial intelligence (AI) based machine learning (ML) and multi-objective optimisation (MOO) models are popular nowadays to acquire the optimal mix design.

ML models such as artificial neural networks (ANN) and support vector regression (SVR) have been utilised extensively in data mining given their excellent generalisation capability, computation speed, and predictive accuracy [28,29]. For instance, the SVR model is capable of handling classification problems, alongside linear or nonlinear tasks. Besides, it can be mapped to a higher dimensional space to compute linear regression functions with reduced complexity [28,30,31].

However, hyperparameters tuning is challenging for ML modelling [32—34]. Typically, the hyperparameters are adjusted by a grid search method, which owns high computational complexity and fails to be applied to address multiparameter problems. Hence, optimisation algorithms have been implemented to auto-search for optimal hyperparameters, for instance, particle swarm optimisation (PSO), genetic algorithm (GA), and firefly algorithm (FA) [35—37]. In this paper, FA is utilised to optimise the hyperparameters of the BPNN and SVR model due to its ability to eliminate the effects of multimodality and achieve automatic segmentation.

By applying MOO theory and metaheuristic algorithm, the FA-based multi-objective optimisation (MOFA) is adopted to optimise the mix design [38—40]. In contrast to the single-objective optimisation method, MOFA enables the simultaneous optimisation of multiple objectives such as compressive strength, ASR expansion, and cost under highly nonlinear constraints via the presented Pareto solutions. Cheng et al. [41] used SVR and GA for the optimisation of high-performance concrete mixes. Zhang et al. [42] optimised three objectives of strength, slump, and cost employing a multi-objective PSO algorithm.

This paper focuses on the effects of mechanical, chemical, hydrothermal, and combined activation on the compressive strength and ASR expansion of mortar samples containing waste glass powder (WGP). Meanwhile, WGP with the mean

particle size of 75 μm and 300 μm was selected as a replacement of fine sand by 10%, 20%, and 30%. The chemical activators consist of sodium sulfate serving as the salt activator, calcium hydroxide and sodium hydroxide serving as alkaline activators. In total, 103 groups of specimens were cast for compressive and ASR expansion tests. A scanning electron microscopy (SEM) machine was utilised to analyze the microstructure of activated WGP. Subsequently, the MOFA was employed to perfect the multi-objective mixture proportions based on the data of UCS, ASR expansion, and the objective function of cost. The sensitivity analysis was also conducted to rank the importance of input variables.

2.   Experimental program

2.1.   Materials

The WGP employed in this test was obtained from transparent waste bottles in a recycling station. The bottles are pretreated by removing labels and contaminants before the crushing process. Afterward, the crushed air-dried bottles were ground into the powder with average particle sizes of 75 m and 300 m through a ball mill. Lastly, the processed WGP was kept in an airtight container. The true density of the WGP is around 2.3–2.5 t/m³ and the appearance of WGP with 75 μm and 300 μm is denoted in Fig. 1.

The ordinary Portland cement category is P.O 42.5R and ground silica sand (over 96% silicon dioxide) is graded as ASTM C778 [43]. The densities of cement and silica sand are 3.0–3.2 t/m³ and 2.3 t/m³, respectively. The fineness index of cement was 390 m²/kg and its normal consistency was 27%. The chemical compositions of the cement and WGP by X-ray Fluorescence Spectrometer (XRF) are demonstrated in Table 1. WGP contains 74.02% silica indicating its excellent potential in terms of pozzolanic behavior [44–46].

2.2.   Mix design and WGP activation

In this research, the variables include the WGP size, the WGP replacement mass ratio, the dosages of chemical additives, and curing time. The levels of these variables are summarised in Table 2. Besides, the water to cement ratio was constantly maintained at 0.45, and the aggregate (WGP + sand) to cement ratio was kept at 2.25. It is noted the hydrothermal and

Table 1 – Chemical compositions of WGP and cement.

Chemical composition	WGP	Cement
SiO$_2$	74.02%	20.10%
Al$_2$O$_3$	1.40%	4.60%
Fe$_2$O$_3$	0.19%	2.80%
CaO	11.25%	63.40%
MgO	3.34%	1.30%
SO$_3$	0.33%	2.70%
Na$_2$O	9.03%	0.60%
K$_2$O	0.29%	—
True density	2.3–2.5 t/m³	3.0–3.2 t/m³
Total chloride	—	0.02%

combined activations are only implemented on samples incorporating 75 μm WGP where the aim is to compare the efficacy of versatile activation approaches. The activation treatment methods adopted are specifically described as follows:

a. Mechanical activation: Waste glass on average 300 μm particle size was ground to 75 μm by a ball mill. The finer glass powder was expected to yield better pozzolanic performance.

b. Chemical activation: The chemical activators were sodium sulfate (NaSO$_4$), calcium hydroxide (Ca(OH)$_2$), and sodium hydroxide (NaOH). Sodium sulfate was utilised as the salt activator, and a mixture of 50% sodium hydroxide and 50% calcium hydroxide was adopted as the alkaline activator. As water-soluble materials, sodium hydroxide and sodium sulfate can be proportionally dissolved in mixed water. Nevertheless, calcium hydroxide is slightly soluble in water requiring prior mixing with WGP and then blended with cement and sand. The mixing procedure for mortar production is as per ASTM C305 [47].

c. Hydrothermal activation: Hydrothermal activation is achieved by steam treatment of WGP at high pressure and temperature. The WGP (75 μm and 300 μm) was hydrothermally processed at 105 °C and 0.143 MPa for 2 h followed by drying in an oven at 80 °C. The dried glass powder exhibited caking and hardening, which necessitated further grind and eventual retention in desiccators.

d. Combined activation: In this approach, the activation methods a, b, and c were united. The chemical activators and WGP were initially mixed completely in water. Afterward, the mixture was shifted to the autoclave for hydrothermal activation as described in method c.

(a) 300μm WGP   (b) 75μm WGP

Fig. 1 – The distinctive features of WGP with the mean particle size of (a) 300 μm and (b) 75 μm.

Table 2 — Variables with all levels used in this experiment.

Variables	Number of levels	Magnitude
WGP size (μm)	2	75, 300
WGP replacement ratio (%)	4	0, 10, 20, 30
Alkali ratio (%)	4	0, 2, 4, 6
Sodium sulfate ratio (%)	4	0, 2, 4, 6
Curing duration (days)	3	7, 14, 28

2.3. Unconfined compressive test

The UCS experiment was performed on the mortar specimens to verify the influence of the different activations and their mix design on the mechanical performance at diverse curing ages. The samples were cast into cubes of size $50 \times 50 \times 50$ mm with three parallel samples per mix design. Following the cast, the samples were rapidly protected by plastic sheets and kept in a humid room for a whole day. Afterward, the specimens were released from molds and maintained in a thermotank for 7, 14, and 28 days. It is essential to ensure that the strength test is applied soon after taking the sample out of the storage tank. A servo-hydraulic testing machine was employed to provide loading rates of 0.6 MPa/s and record ultimate strengths. The experiment results are summarised in the Appendix.

2.4. Alkali silica reaction (ASR)

The degree of ASR expansion as specified in ASTM C1260 [48] was assessed by calculating the longitudinal variation of mortar bar specimens. Three parallel specimens were manufactured for each mixture and the final results were recorded as the average longitudinal rate of change. The prismatic specimens were cast into the size of $25 \times 25 \times 280$ mm equipped with two steel stud gauges at both ends (effective length 260 mm). According to ASTM C1260 [48], a high temperature of 80 °C and 1N sodium hydroxide (NaOH) solution were applied to accelerate ASR. After casting, the molds were rapidly placed in a humid room to cure for 24 h. Then, the specimens were demolded and soaked in water of 80 °C for another whole day. The length of the immersed bar sample was defined as the initial length L_0. Subsequently, the bar samples were shifted to NaOH solution at 80 °C and measured for length at 2, 4, 7, 10, and 14 days. The length at day x is represented by L_x. It is noted that the measurement is supposed to be completed within 15±5s of taking samples out of the alkali solution. A length comparator and a digital indicator were utilised to gauge the length of bars and the ASR expansion ratio e was derived by Eq. (1). The ASR experimental results are summarised in the Appendix.

$$e = \frac{L_x - L_0}{260} \times 100\% \qquad (1)$$

2.5. Scanning electron microscopy (SEM)

A scanning electron microscopy (SEM) apparatus was applied to visually investigate the microstructure of the activated WGP. To observe the chemical erosion in the WGP surface, a 50g WGP sample (75 μm) was soaked in 100 ml water mixed with 4.3g sodium sulfate and 4.3g alkali. The hydrothermal and combined activations were also conducted on another 50g WGP samples to explore the microstructural morphology.

3. Multi-objective optimisation methodology

The optimal mixture design of activated WGP mortar adopts the methodology of MOFA-SVR. The process is depicted in Fig. 2. Overall, this multi-objective design started from the construction of two RF models for the prediction of UCS and ASR with the hyperparameters tuned by FA and 10-fold cross-validation (CV). Then, the cost was calculated for each mix. The weighted sum method was used for establishing a multi-objective function and the Pareto front was produced to show the optimisation mixture design of WGP mortar.

3.1. Data description

As mentioned above, the variables are the size and proportion of WGP, the content of chemical activators, and the curing time. The dataset is sourced from the results from UCS and ASR expansion tests and they are served as the output variables. The statistics of input and output variables are listed in Table 3 for UCS and Table 4 for ASR expansion.

The figures of correlation between different input variables of UCS and ASR datasets are shown in Fig. 3. The correlation between sand and WGP was high because the WGP was in replacement of sand by 10%—30%. Therefore, the ratio of WGP to sand and cement was used to conduct the variable importance analysis. While for multi-objective optimisation (MOO) analysis, the amount of each raw material had to be represented instead of the ratio. The other correlation values were low enough that the input variables were independent so that the multicollinearity problems could be effectively eliminated in this study.

3.2. Establishment of FA-SVR model

3.2.1. Support vector regression (SVR)

SVR was first established by Vapnik (1995). The Kernel function defined in SVR can organize data from the sample space to the higher dimensional space to solve the nonlinear problems. The sample is described as (x_i, y_i) where x_i is a one-dimensional vector representing the features and y_i is the actual sample value. The sample space comprising n samples is described in Eq. (2) and the regression function is written as Eq. (3).

$$\{(x_1, y_1), (x_2, y_2), \ldots, (x_n, y_n)\} \qquad (2)$$

$$f(x) = w \cdot \varphi(x) + \beta \qquad (3)$$

where w and β are the weight vector and bias; $\varphi(x)$ is a mapping function. The loss function is defined as Eq. (4) which represents the error between prediction $f(x_i)$ and actual value y_i.

$$\mathscr{L}(x, y, f) = |y_i - f(x_i)|_e = \begin{cases} 0, & |y_i - f(x_i)| < e \\ |y_i - f(x_i)| - e_i, & |y_i - f(x_i)| \geq e \end{cases} \qquad (4)$$

where e means the largest tolerance error so that the training point will not be penalised if it is within the e-tube. The
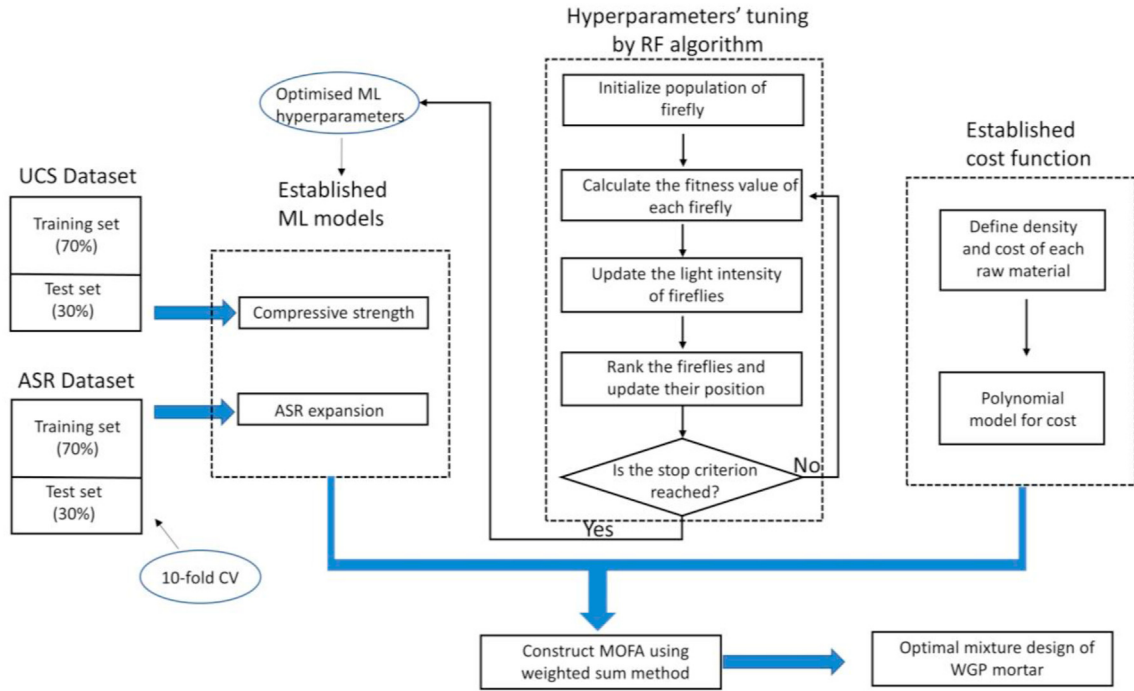
Fig. 2 − Flowchart of the MOFA on the design of WGP-mortar.

problem can be described as Eq. (5) according to the minimal structural risk [49].

$$\mathscr{R}(w) = \frac{1}{2}\|w\|^2 + \sum_{i=1}^{n} \mathscr{L}(x, y, f) \tag{5}$$

To improve tolerance for biased data, the slack variables δ_i and δ_i^* are introduced to deal with infeasible constraints. Eq. (5) can be rewritten into the following convex optimisation equation:

$$min_{w,e,\delta,\delta^*} \mathscr{R}(w) = \frac{1}{2}w^2 + C\sum_{i=1}^{n}(\delta_i + \delta_i^*)$$

$$s.t \begin{cases} y_i - w\cdot\varphi(x) - \beta \leq e + \delta_i \\ w\cdot\varphi(x) + \beta - y_i \leq e + \delta_i^* \\ \delta_i \geq 0 \\ \delta_i^* \geq 0 \end{cases} \tag{6}$$

where C is a penalty parameter to evaluate the penalising degree of the difference between the regression curve and the samples out of the e-tube.

Fig. 4 presents a schematic diagram of a nonlinear SVR. Subsequently, the positive Lagrange multipliers (α_i, α_i^*, u_i, u_i^*) are introduced to deal with varying constraints, as shown in Eq. (7).

$$L(w, \beta, \delta, a, u) = \frac{1}{2}w^2 + C\sum_{i=1}^{n}(\delta_i + \delta_i^*)$$

$$- \sum_{i=1}^{n} a_i(e + \delta_i - y_i + w\cdot\varphi(x_i) + \beta)$$

$$- \sum_{i=1}^{n} a_i^*(e + \delta_i + y_i - w\cdot\varphi(x_i) - \beta) \tag{7}$$

$$- \sum_{i=1}^{n}(u_i\delta_i + u_i^*\delta_i^*)$$

When the constraints are seriously opposite to each other, and the objective equation is differentiable, the Karush-Kuhn-Tuck (KKT) rules need to be satisfied for each of the prime and dual points in Eq. (8) [50]. According to the KKT, the product of dual variables and constraints in the optimal solution is 0 as shown in Eq. (9).

Table 3 − Statistics of input and output variables for the UCS dataset.

Variables	Notation	Minimum	Maximum	Median	Std Dev
Glass powder (kg/m³)	WGP	0	303.75	202.50	84.75
WGP size (μm)	Z	75	300	75	112.49
Sodium sulfate (kg/m³)	S	0	27	9	10.02
Alkali (kg/m³)	H	0	27	9	10.02
Sand (kg/m³)	D	708.75	1012.50	810	84.75
Age (day)	A	7	28	14	8.73
Compressive strength (MPa)	UCS	6.82	36.53	19.17	5.91

Table 4 – Statistics of input and output variables for the ASR dataset.

Variables	Notation	Minimum	Maximum	Median	Std Dev
Glass powder (kg/m^3)	WGP	0	303.75	202.50	84.75
WGP size (μm)	Z	75	300	75	112.49
Sodium sulfate (kg/m^3)	S	0	27	9	10.02
Alkali (kg/m^3)	H	0	27	9	10.02
Sand (kg/m^3)	D	708.75	1012.50	810	84.75
Age (day)	A	2	14	7	4.27
Alkali-silica reaction expansion (%)	ASR	0.001	0.144	0.059	0.034

$$\begin{cases} \dfrac{\partial L}{\partial w} = w - \sum_{i=1}^{n} \left(a_i - a_i^* \right) \varphi(x_i) = 0 \\[2mm] \dfrac{\partial L}{\partial \beta} = \sum_{i=1}^{n} \left(a_i - a_i^* \right) = 0 \\[2mm] C - a_i - u_i = 0 \\[2mm] C - a_i^* - u_i^* = 0 \end{cases} \quad (8)$$

$$\begin{aligned} & a_i \left(e + \delta_i - y_i + w \cdot \varphi(x_i) + \beta \right) = 0 \\ & a_i^* \left(e + \delta_i + y_i - w \cdot \varphi(x_i) - \beta \right) = 0 \\ & (C - a_i)\delta_i = 0 \\ & (C - a_i^*)\delta_i^* = 0 \end{aligned} \quad (9)$$

The Langrage dual problem can be finally derived by solving the above equations.

$$\begin{aligned} max_i & \left(-\frac{1}{2}\sum_{i=1}^{n}\sum_{j=1}^{n}\left(a_i - a_i^*\right)\left(a_j - a_j^*\right)x_j^T x_j \right. \\ & \left. - e\sum_{i=1}^{n}\left(a_i - a_i^*\right) + \sum_{i=1}^{n}y_i\left(a_i - a_i^*\right)\right) s.t \begin{cases} \sum_{i=1}^{n}\left(a_i - a_i^*\right) = 0 \\ a_i, a_i^* \in [0, C] \end{cases} \end{aligned} \quad (10)$$

According to Eq. (9), w can be calculated as $\sum_{i=1}^{n}(a_i - a_i^*)\varphi(x_i)$, and the regression function is shown as follows:

$$f(x) = \sum_{i=1}^{n}\left(a_i - a_i^*\right)\varphi(x_i)x + \beta \quad (11)$$

3.2.2. Back-propagation neural network (BPNN)

BPNN is commonly composed of an input layer, one or more hidden layers, and one output layer. The neural network employs interlinked neurons to establish the relationships between inputs and outputs. The output (O) is represented as follows:

$$O = f\left(\sum_{j=1}^{n}\left(w_j x_j\right) + b\right) \quad (12)$$

where w_j is the weight value of the jth input neuron (x_j) in the former layer; b is the bias value; f is the activation function shown in Eq. (13).

$$f(x) = \frac{2}{1 + \exp(-x)} - 1 \quad (13)$$

The back-propagation process is used to adjust the weight values and thresholds. This can be achieved by computing the gradient of the weighting error function. The training iteration will stop when the mean square error (MSE) between the actual and predicted outputs become smaller than a defined threshold. The sketch diagram of the back-propagation process is shown in Fig. 5.

Besides, logistic regression (LR) and multiple linear regression (MLR) were also trained as the baseline models. The specific algorithm description can be found in other research papers [35].

3.2.3. Firefly algorithm

For the SVR, two basic hyperparameters (Gaussian kernel parameter γ and namely penalty coefficient c) need to be tuned by FA. As regards BPNN, the hyperparameters are the amounts of hidden layers and neurons in each layer. The FA is inspired by the social behaviour of fireflies. Fireflies are attracted to the brightness so that the attractiveness is in a positive relationship to the brightness of the firefly. The attractiveness of brightness decreases as the distance
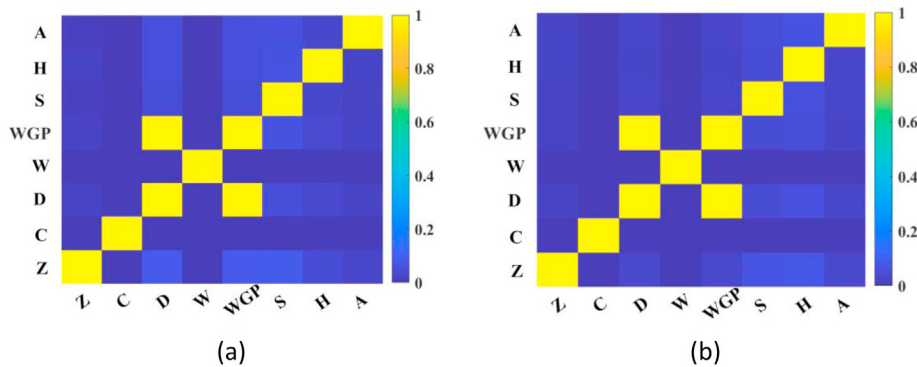

(a)   (b)

Fig. 3 – Correlation matrix of input variables for (a) UCS dataset (b) ASR dataset.
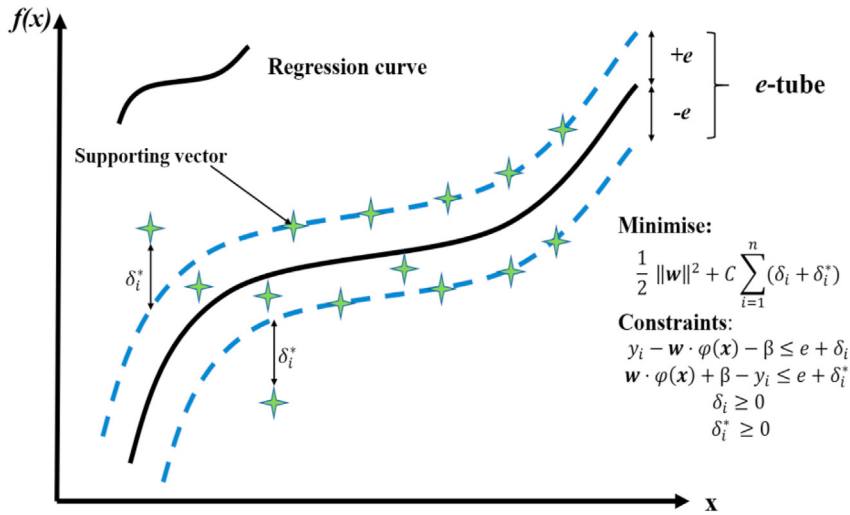
Fig. 4 – A support vector regression machine.

between two fireflies increases. The brightest firefly flies randomly through the surrounding area. Eventually, the brightest firefly can be deduced when the other fireflies continuously travel towards it. The brightness can be written as a fitness function based on a concrete problem. Eq. (14) shows the changed position x_i^{t+1} when firefly i moves towards firefly j.

$$x_i^{t+1} = x_i^t + \beta_0 e^{-\gamma r_{ij}^2}\left(x_j^t - x_i^t\right) + \alpha(rand - 1/2) \tag{14}$$

$$r_{ij} = \left\|x_j^t - x_i^t\right\| \tag{15}$$

where x_i^t and x_j^t are the positions of two fireflies i and j at the t-th iteration; r_{ij} in Eq. (15) shows the Euclidian distance between fireflies i and j; β_0 is the highest attractiveness of the firefly when r equals zero; α and $rand$ are the randomization parameter and random vector derived from the Gaussian distribution, ranging from 0 to 1. The γ (ranging from 0 to 1) is introduced (an absorption coefficient) to represent the situation that the brightness reduces with distance and medium. The pseudocode of FA can be shown in Fig. 6.

3.3. Hyperparameter tuning

3.3.1. Cross fold validation
A 10-fold CV was used in this study to assess the data, eliminating the overfitting problems. The experimental dataset was randomly divided into two groups comprising testing set (accounting for 30%) and training set (accounting for 70%). The training set was then split into 10 folds (9 for ML training, and 1 for the validation of the model performance), as shown in Fig. 7. The hyperparameters were iterated for 50 times according to the root mean square error (RMSE) obtained after each validation. The above process was repeated 10 times with a non-repetitive validation fold chosen at each time. Ultimately, the trained ML model with optimal hyperparameters would be used to test the model performance on the training set.

3.3.2. Performance assessment
Evaluation is essential in measuring the accuracy of the model. In this research, RMSE, MAE, correlation coefficient (R), and mean absolute percentage error (MAPE) were the evaluation indices. They are defined in the following equations.

$$RSME = \sqrt{\frac{1}{n}\sum_{i=1}^{n}\left(y_i^* - y_i\right)^2} \tag{16}$$

$$MAE = \frac{1}{n}\sum_{i=1}^{n}|y_i^* - y_i| \tag{17}$$

$$MAPE = \frac{1}{n}\sum_{i=1}^{n}\left|\frac{y_i^* - y_i}{y_i}\right| \tag{18}$$

$$R = \frac{\sum_{i=1}^{n}\left(y_i^* - \overline{y^*}\right)\left(y_i - \overline{y}\right)}{\sqrt{\sum_{i=1}^{n}\left(y_i^* - \overline{y^*}\right)^2}\sqrt{\sum_{i=1}^{n}\left(y_i^* - \overline{y}\right)^2}} \tag{19}$$

where n means the n groups of data samples; y_i^* and y_i demonstrate the predicted and actual values; $\overline{y^*}$ and $\overline{y}$ are the mean values of the predicted and actual data, respectively.

3.4. Multi-objective optimisation

3.4.1. Objective function establishment
The cost was also included for the MOO design. A polynomial function shown in Eq. (20) was used to calculate the cost of mortar containing WGP.

$$Cost(\$/m^3) = C_c Q_c + C_w Q_w + C_D Q_D + C_{WGP}Q_{WGP} + C_S Q_S + C_H Q_H \tag{20}$$

In the above equation, C is the unit price (\$/kg) of the materials used in mortar production and Q represents the quantity (kg/m³) of different raw materials. The cost of cement, water, silica sand, WGP, and chemical activators is listed in Table 5 in which all the prices are the average local retailing price.
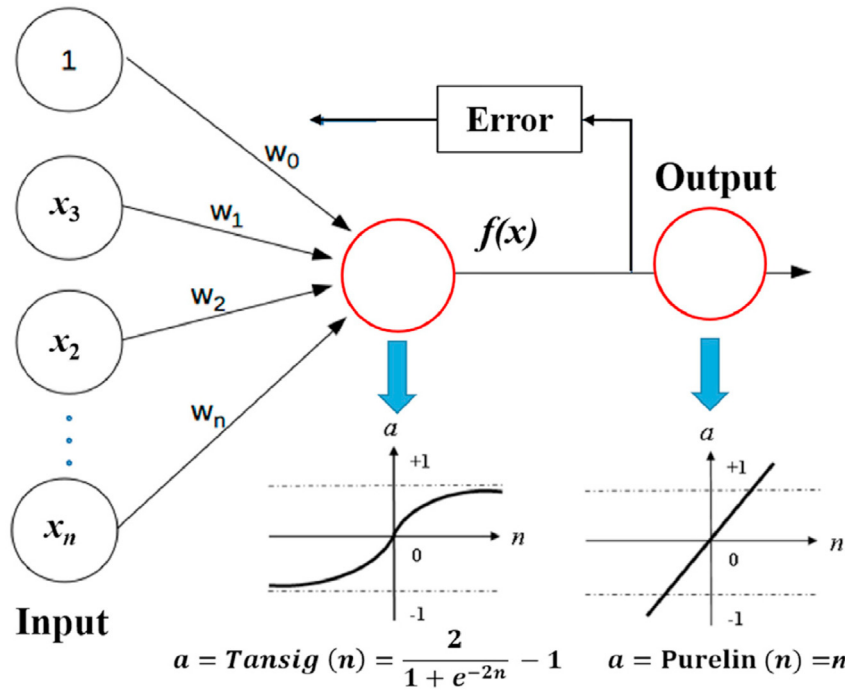
Fig. 5 — Back-propagation in the BPNN [35].

3.4.2. Constraints of variables

To solve multi-objective optimisation problems, several constraints are set including mortar volume constraint, range constraint of materials, and ratio constraint, shown in Eq. (21) and Table 6. The price of WGP mortar is calculated based on one cubic meter to unify the unit. The input variables are summarised for their minimum and maximum values and three ratio constraints are also determined for calculating Pareto optimal solutions.

$$V_m(1m^3) = \frac{Q_c}{U_c} + \frac{Q_w}{U_w} + \frac{Q_D}{U_d} + \frac{Q_G}{U_G} + \frac{Q_S}{U_S} + \frac{Q_H}{U_H} \qquad (21)$$

where U is the unit weight of materials.

```
Begin
Define objective function  f(x),  x = (x₁, … , x_d)ᵀ
Set the search space, total number of generations, and fireflies
Obtain light intensity  Iᵢ  at  xᵢ  by  f(xᵢ)
Set light absorption coefficient
Generate initial population,  k = 0
While (t ≤ maxGeneration) do
        Update the generation number,  k = k + 1
        Tune randomisation parameter using adaptive inertia weight
        Tune attractiveness parameter using Guass/mouse chaotic map
            for  i = 1  : no. fireflies
                for  j = 1  : no. fireflies
                    if (I_j > Iᵢ)
                            move firefly  i  toward  j  by levy flight
                    end if
                    change attractiveness with distance  r
                end for  j
            end for  i
            Rank the fireflies and find the current best
end while
Obtain results
End
```
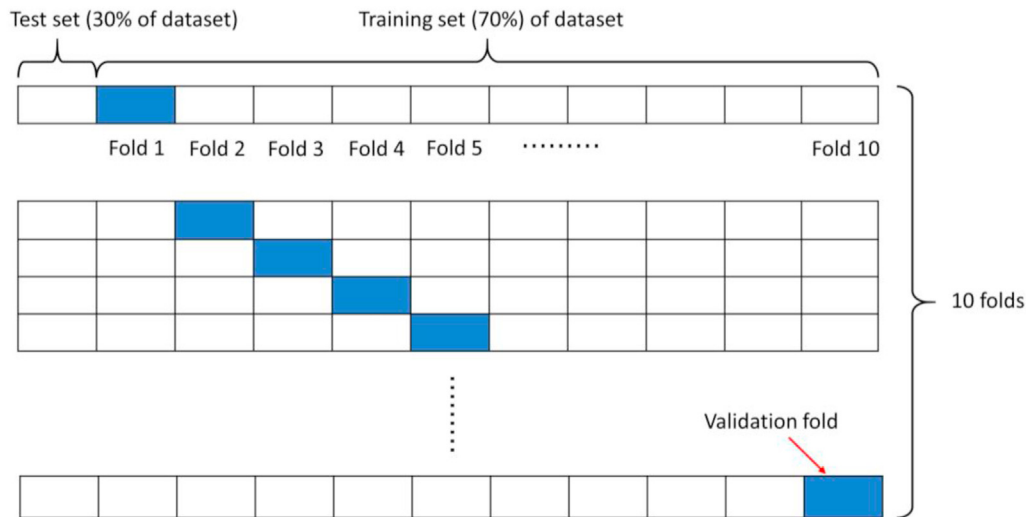
Fig. 6 — The pseudocode of FA.

Fig. 7 – 10-fold cross-validation.

3.4.3. Construction of MOFA

The establishment of MOFA is based on the objective functions of UCS, ASR, and cost by applying the weighted sum method. The UCS and ASR are combined with cost separately to set up a function as shown in Eq. (22).

$$f = \sum_{i=1}^{i} w_i f_i, \sum_{i=1}^{i} w_i = 1 \qquad (22)$$

where f_i means the multiple objectives; f is the combined function in solving MOO problem; w_i equals to p_i/i where the denominator is the random number arising from a uniform distribution [0,1] and the numerator is the uniformly distributed number.

The above equation can be formulated in the following manner in this research.

$$F_1 = w_1 \cdot UCS(28\ days) + w_2 \cdot ASR(14\ days) \\ + w_3 \cdot cost,\ for\ 300\mu m\ WGP \qquad (23)$$

$$F_2 = w_1 \cdot UCS(28\ days) + w_2 \cdot ASR(14\ days) \\ + w_3 \cdot cost,\ for\ 75\mu m\ WGP \qquad (24)$$

$$\sum_{i=1}^{3} w_i = 1 \qquad (25)$$

To solve the optimisation problem, Pareto optimal front is determined since the multiple objectives are supposed to be minimised simultaneously. They represent the solutions that are non-dominated so that any of the other objective functions fail to be improved without harming another function. The mathematical expression for Pareto optimum is formed as follows [51,52].

If $x^* \in S$ is Pareto optimal solution, whereby S is the set of feasible solutions, the nonexistence of $x \in S$ such that

$$f_i(\mathbf{x}) \leq f_i(\mathbf{x}^*) \, for\, i = 1, 2, 3, ..., k\, and \qquad (26)$$

$$f_i(\mathbf{x}) < f_i(\mathbf{x}^*) \, for\, at\, least\, one\, value\, i \qquad (27)$$

The set of the non-dominated Pareto optimal solutions constitutes the Pareto optimal front, as shown in Fig. 8. Apart from the Pareto front, the other feasible points would not be optimal since their objective function values are larger than at least one point in the Pareto front. The FA can be developed to MOFA to calculate Pareto optimal solutions for finding optimisation mixture design. The pseudocode of MOFA is summarised in Fig. 9.

3.4.4. Decision-making by TOPSIS theory

Pareto front outputs many non-dominating solutions, while it fails to deal with the best one within these solutions. Thereby, a multi-criteria decision strategy is proposed, which is the technique for order preference by similarity to an ideal solution (TOPSIS) [53]. According to the Pareto solutions, the positive and negative ideal points can be determined. The

Table 5 – Unit price and unit weight of each raw material.

Materials	Notation	Unit Price ($/kg)	Unit weight (kg/m³)
Cement	C_c	0.061	3100
Water	C_w	0.001	1000
Sand	C_D	0.012	2350
Waste glass powder	C_{WGP}	0.089	2450
Sodium sulfate	C_S	0.17	2680
Alkali	C_H	0.21	2190

Table 6 – Constraints of input variables.

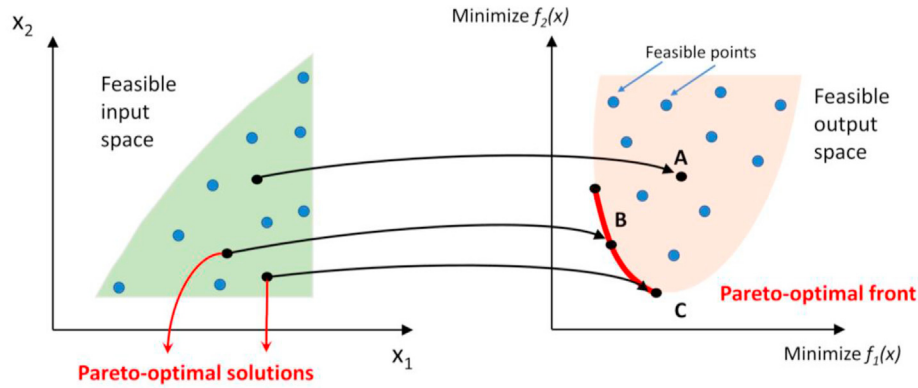| Variables	Expressions	Lower bound	Upper bound
WGP size	S	75	300
Sodium sulfate	C_S	0	27
Alkali	C_H	0	27
WGP ratio	$C_{WGP}/(C_{WGP}+C_D)$	0.1	0.3
WGP and sand to cement ratio	$C_c/(C_{WGP}+C_D)$	0.42	0.46

Fig. 8 – The schematic diagram of Pareto optimal solutions.

realisation of TOPSIS is to select a solution that is closest to the positive ideal point and farthest from the negative ideal point. The positive one is the solution in which the fitness function value is the most ideal and the negative one corresponds to the worst fitness function value. This can be represented by the following equations that a solution with the highest C_i is considered as the best one.

$$d_{i+} = \sqrt{\sum_{j=1}^{n} \left(F_{ij} - F_j^{ideal} \right)^2} \tag{28}$$

$$d_{i-} = \sqrt{\sum_{j=1}^{n} \left(F_{ij} - F_j^{non-ideal} \right)^2} \tag{29}$$

$$C_i = \frac{d_{i-}}{d_{i+} + d_{i-}} \tag{30}$$

where d_{i+} and d_{i-} are the positive and negative ideal solutions; n and i are the numbers of objectives and the ith Pareto point; F_j^{ideal} is the ideal value of the jth objective and $F_j^{non-ideal}$ is the non-ideal value.

3.5.   Variable importance measure

In some cases where the relationship between variables and objectives is nonlinear and complex, the visualisation of their relationship is hard to analyse. Hence, this study used a method based on sensitivity analysis (SA) to rank the important degree of the input variables on the outputs. This is

```
Begin
Define objective function  f₁(x), f₂(x), …, f_k(x); x = (x₁, …, x_d)ᵀ
Generate initial population of fireflies  x_i = (i = 1,2, …, n)
Determine light intensity  I_i  at  x_i  by  f(x₁)
Set light absorption coefficient
While
        for  i, j = 1: n  (all n fireflies)
                Evaluate the approximations of  PF_i  and  PF_j  to the Pareto front
                        if  PF_j  dominates  PF_i,
                                Move firefly from  i  to  j
                                Generate new ones if constraints are not satisfied
                        end if
                        if no non-dominated solutions can be found
                                Generate random weights  w_k(k = 1, …K)
                                Find  the  best  solution  that  can  minimise  the  combined
objective
                                Random walk around the best solution
                        end if
                        Update and pass the non-dominated solutions to the next iterations
                end
                Sort and find the current best approximation to the Pareto front
                Update  t
end while
Post process results and visualisation
```

Fig. 9 – The pseudocode of MOFA.

commonly used to qualitatively or quantitatively evaluate the dependence of outputs on variables by computing the change in output values caused by inputs' variation. In this study, global sensitivity analysis was utilised because it allows multiple variables to be altered simultaneously compared with local sensitivity analysis. In the following equations, the variable 'a' changes in the range of the experimental dataset while the other variables remain constant at their mean values.

$$G_a = \sum_{j=2}^{N} \frac{\left| \widehat{y_{a,j}} - \widehat{y_{a,j-1}} \right|}{N-1} \qquad (31)$$

$$R_a = G_a \bigg/ \sum_{i=1}^{I} G_i \qquad (32)$$

where G_a is the average difference between adjacent outputs $\widehat{y_{a,j}}$ and $\widehat{y_{a,j-1}}$; N is the number of the value of the variable under research; R_a is the relative importance of the variable 'a'.
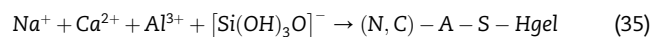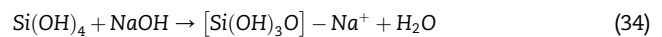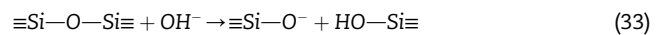
4. Results and discussions

4.1. UCS results

The UCS values of specimens containing 300 μm WGP at the early stage (7 days) and late stage (28 days) are depicted in Fig. 10a and (b), respectively. Meanwhile, the effects of sodium sulfate content, alkali content, and WGP replacement ratio on UCS are intuitively compared. The UCS of WGP mortar samples without chemical agents presented decreasing trend when the WGP replacement ratio increased from 0% to 30% for both early and late curing stages. Statistically, the compressive strength decreased from 26.84 MPa to 21.69 MPa when the WGP ratio increased from 0% to 30%, around 19% lower than the control sample. This weakening tendency was consistent with the previous researches finding illustrating the negative effect of WGP on mechanical strength [54,55]. The possible reasons are excessive ASR expansion which would be concretely discussed in the next section and low pozzolanic reactive arising from its stable silica tetrahedron structure. In this case, less calcium silicate hydrate (C–S–H) or calcium aluminate hydrate (C-A-H) can be generated attributed to the few silicon and aluminum dissolutions. Meanwhile, the interfacial transition zone between hydration product and glass powder is weaker than that between cement hydrates and sand because of the smoother glass surface. Therefore, the mechanical strength was decreased by the WGP addition.

Regarding the contents of chemical additives, the main trend between UCS and agents' contents could be observed despite of some fluctuations which were probably caused by the experimental error. Generally, sodium sulfate at 2% resulted in the maximum UCS. Besides, alkali content ranging from 0% to 2% led to relatively higher UCS. However, the excessive contents of both sodium sulfate and alkali caused significant compressive strength diminishment. In Fig. 10b, the efficacy of chemical agents (at appropriate dosage) has been verified to at least enhance the UCS of WGP sample to the strength level of the control sample. The mechanisms of UCS

improvement by sodium sulfate and alkali are mainly attributed to the WGP structure depolymerisation and WGP-cement system excitation.

The alkali additive provided additional hydroxide ions apart from those derived from the cement hydration. As mentioned before, the stable silica tetrahedron structure of the glass powder hinders the dissolution of silica and aluminum, reducing its pozzolanic reaction. However, the stable structure is prone to be destroyed under high alkali concentrations [56]. This is because the glass solution is weakly acidic (silicon dioxide is acidic oxide) and the chemical bonds between silicon/aluminum and oxygen atom are weak to be broken under high alkali concentration [56]. Specifically, the chemical bond fracture can be described in the following equations.

$$\equiv Si-O-Si \equiv + OH^- \rightarrow \equiv Si-O^- + HO-Si \equiv \qquad (33)$$

$$Si(OH)_4 + NaOH \rightarrow [Si(OH)_3O] - Na^+ + H_2O \qquad (34)$$

$$Na^+ + Ca^{2+} + Al^{3+} + [Si(OH)_3O]^- \rightarrow (N,C) - A - S - Hgel \qquad (35)$$

Eq. (35) demonstrates the possible formation of gels in the alkali-activated WGP-cement system. Nevertheless, this gel product is highly dependent on the WGP reactivity and the availability of sodium, calcium, and aluminum [57,58]. As a result, one of the most important contributions from alkali addition is WGP structural depolimerisation for active silicon and aluminum dissolution into further pozzolanic reaction. Way and Shayan [59] also stated the positive relationship between silica concentration in solution and the addition of alkali hydroxide. Besides, alkali can also active the cement system by increasing the PH value, especially at an early age, resulting in a shorter dormant period of cement hydration and a faster hydration rate [59]. However, the effect of alkali additive on UCS of 300 μm WGP mortar was very limited and even negative when the alkali content was higher than 2% (see Fig. 10). Some researchers observed a similar phenomenon and attributed it to heterogeneous gel formation and reduction of calcium ion concentration [56,60]. Another possible reason is excessive ASR expansion which is specifically discussed in the next section.

As regards the sodium sulfate efficacy, it can be regarded as the combination of alkali excitation (owing to Na^+) and sulfate excitation (owing to SO_4^{2-}) [61,62]. Similar to the fly ash-cement system, the chemical reaction can be presented in the following equations. Apart from the alkali activation mentioned above, the gypsum ($CaSO_4$) can be generated to react with aluminate (C_3A) to form ettringite (AFt). The increased amount of AFt can enhance the mortar density and simultaneously improve the early mechanical strength. In addition, the alite (C_3S) hydration can also be accelerated by sulfate ions to generate C–S–H gels. Nevertheless, too much sulfate inevitably leads to excessive AFt to causing the loose structure and reducing the mortar robustness. This is consistent with the phenomenon in Fig. 10 that the UCS exhibited a downward trend when the sodium sulfate content was higher than 2%.
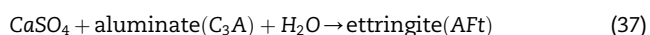
$$Na_2SO_4 + Ca(OH)_2 \rightarrow CaSO_4 (gypsum) + NaOH \qquad (36)$$
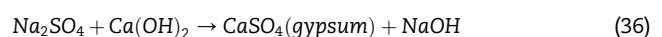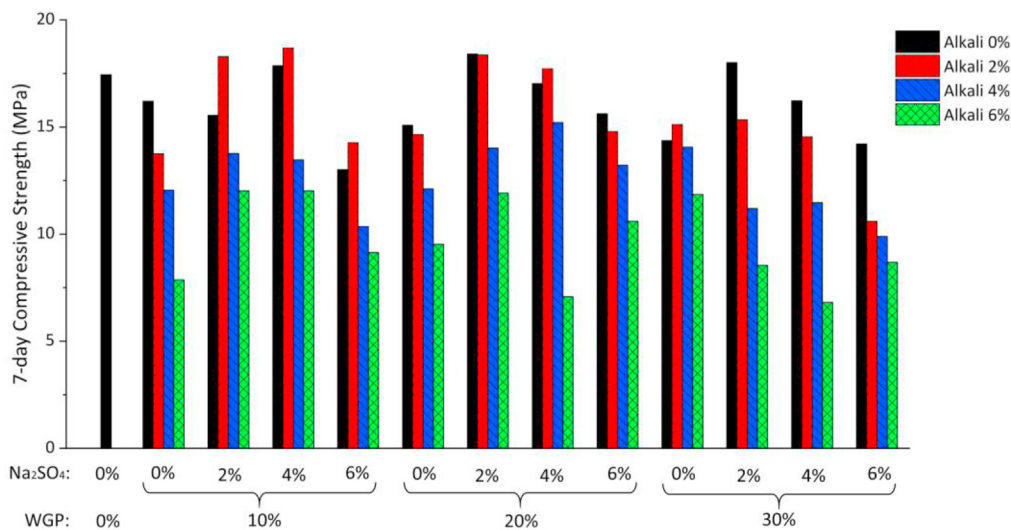
(a)
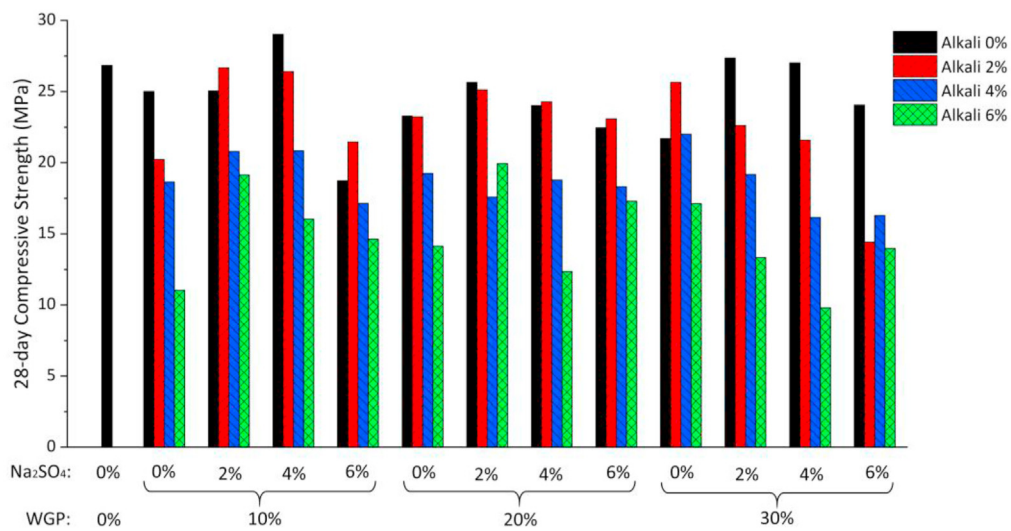
(b)

Fig. 10 − 7-day (a) and 28-day (b) UCS of specimens containing WGP (300 μm) chemically activated by different dosages of sodium sulfate and alkali.

$$CaSO_4 + \text{aluminate}(C_3A) + H_2O \rightarrow \text{ettringite}(AFt) \qquad (37)$$

Apart from the chemical activation, mechanical grinding is another feasible method to activate waste glass. Through the grinding process, the stable silica tetrahedron structure of the glass is prone to be broken, leading to a reduced degree of crystallization (the tendency from crystallisation to amorphousness) [63,64]. Meanwhile, the specific surface area of WGP can be increased to enhance the WGP pozzolanic potential. The density of the WGP mortar is also increased owing to the uniform distribution of tiny WGP in the pores of mortar. Thereby, the mechanical performance of WGP mortar is supposed to be improved after mechanical grinding. Fig. 11 depicts the UCS variations for specimens containing 75 μm WGP with and without chemical activation. The 28-day UCS was

26.84 MPa for the control sample, which increased to 35.72 MPa, 27.90 MPa, 31.88 MPa, respectively when was 10wt %, 20wt%, and 30wt% sand was replaced by 75 μm WGP. This improved UCS verified the positive efficacy of mechanical grinding. Similar to 300 μm WGP mortar, the chemical additives' threshold (2% for both alkali and sodium sulfate) was also pronounced for most 75 μm WGP mortar samples. However, the moderate content of chemical additives (i.e., ≤2%) is capable of improving the compressive strength. The highest 28-day UCS (35.33 MPa) was found on mortar sample incorporation 75 μm WGP (30%), alkali (2%), and sodium sulfate (2%).

The hydrothermal activation was also investigated as supplementary. Fig. 12 shows the UCS of samples with versatile curing times and WGP replacement ratios, presenting
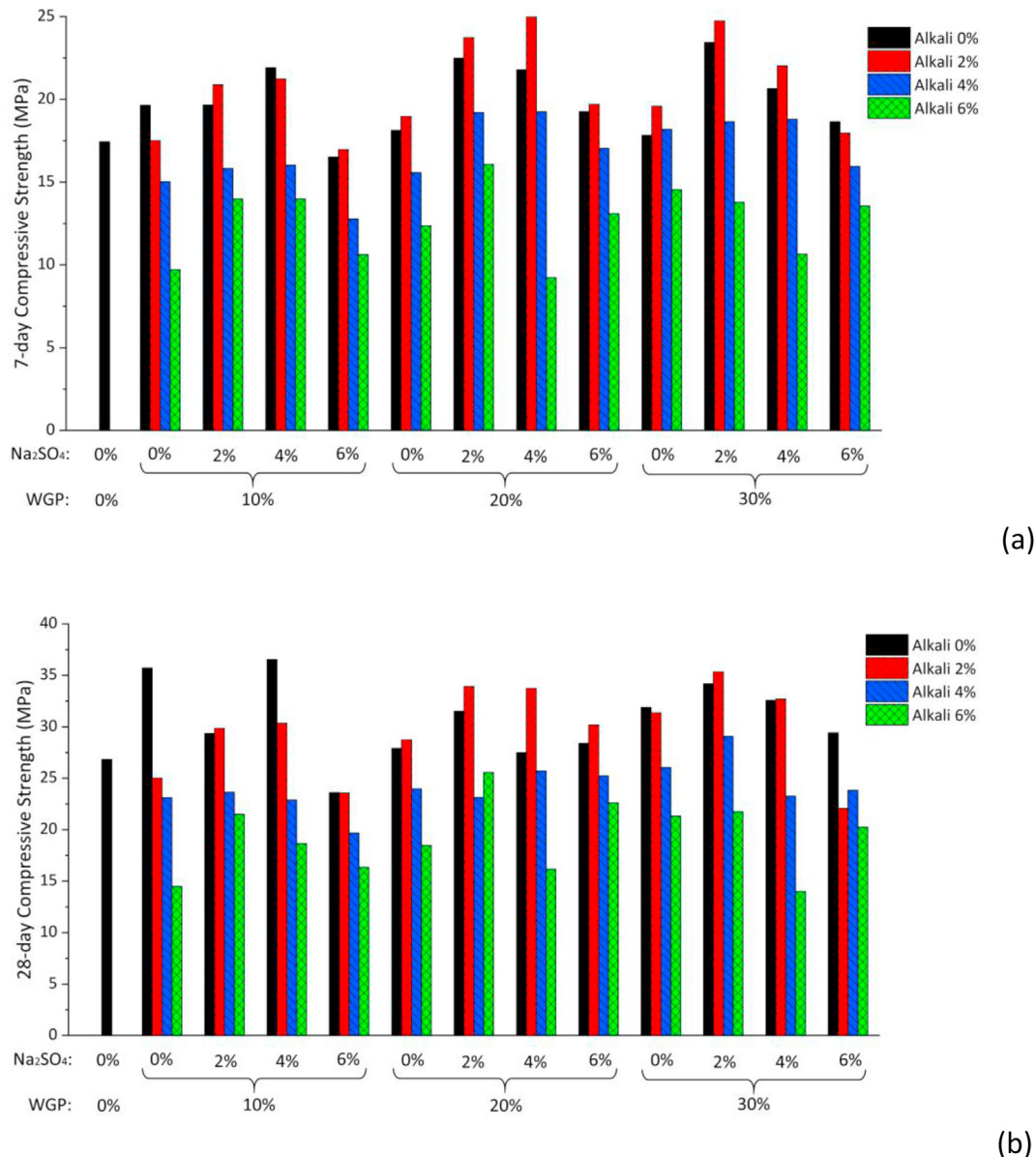
(a)

(b)

Fig. 11 — 7-day (a) and 28-day (b) UCS of specimens containing WGP (75 μm) chemically activated by different dosages of sodium sulfate and alkali.

the efficacy variance of four activation methods (NA, C, H, and CH). It is noted that the chemical additive in Fig. 12 was the mixture of 2% alkali and 2% sodium sulfate which was considered as the optimal one according to the previous description. The increased UCS demonstrated the positive efficacy of hydrothermal activation. Regarding the mechanism of hydrothermal activation, it can break the chemical bond and reduce the WGP structural stability through high temperature and pressure (105 °C and 0.143 MPa in this study). The Silica tetrahedron units can be depolymerised as presented in Eq. (38) [65,66]. However, the $Si(OH)_4$ is prone to adhere to the glass surface (silica gel membrane) after being polarized by water molecules, hindering the hydrothermal reaction. The alkali can neutrally react with silica gel, contributing to the WGP depolymerisation. Therefore, the

alkali within the hydrothermal process is essential, otherwise, the hydrothermal duration cannot be long.

$$\equiv Si-O-Si\equiv + H-O-H \rightarrow \equiv Si-OH + HO-Si\equiv \qquad (38)$$
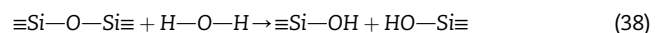
In general, the chemical activation outperformed hydrothermal activation at an early age. However, the gap between chemical and hydrothermal activations is gradually narrowed at a late stage (i.e., 28 days). Compared to the un-activated 30% WGP (75 μm) sample, the 28-day UCS increased from 31.88 MPa to 35.33 MPa and 35.13 MPa, respectively, corresponding to chemical activation and hydrothermal activation. Besides, the combined activation has the benefit of obtaining adequate strength at both early and late ages. As mentioned before, this might be attributed to the alkali addition in the hydrothermal process which promoted the WGP structural
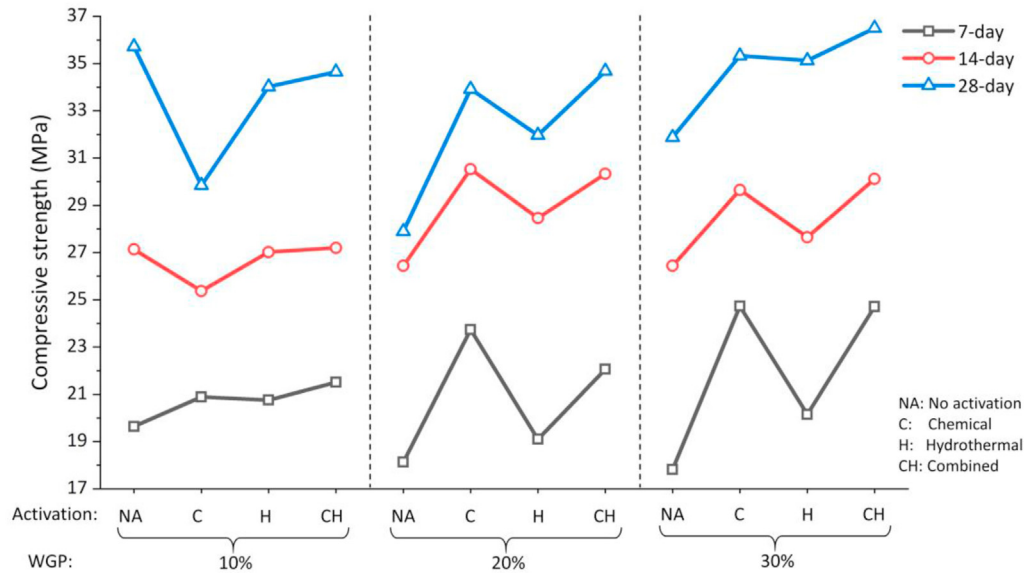
Fig. 12 — The effect of activation approaches on UCS of specimens containing 75 μm WGP at varying curing ages.

fracture. Furthermore, the 30% WGP (75 μm) with combined activation is the optimal choice. The specimen containing such WGP showed a UCS of 36.5 MPa, about 14% and 36% larger than that of the non-activated 30% WGP specimen and control sample, respectively.

4.2. ASR expansion results

Fig. 13 depicts the 14-day ASR expansion outcomes for specimens containing versatile contents of 300 μm and 75 μm WGPs. The influence of alkali and sodium sulfate on ASR expansion is also intuitively compared in this figure. The mechanism of ASR is attributed to the formation of ASR gel which is capable of swelling when it absorbs water. The ASR gels can be generated around the glass surface provided the alkali concentration is high and the silica is reactive.

As to 300 μm WGP mortar without chemical activation, the ASR expansion exhibited a rising trend by increasing WGP content. When the glass replacement was 30%, the expansion reached 0.144% at 14days, exceeding the ASTM threshold (0.1%). This finding was consistent with previous publications, demonstrating the detrimental effect of coarse glass particles in concrete. Regarding 75 μm WGP mortar without chemical activation, the ASR expansion was mitigated compared to the control sample. Shayan and Xu [67] explained that the fine WGP was prone to have a pozzolanic reaction to generate non-swelling gels. The threshold of the WGP size is reported by some researchers as 0.15–0.30 mm [15,67]. However, the expansion of 30% 75 μm WGP specimen exceeded the ASTM threshold, which was similar to that of specimen containing 30% coarse WGP. This phenomenon contradicted the previous finding that fine glass powder was harmless to ASR expansion. Du and Tan [15] attributed the ASR expansion to the micro-cracks in glass particles, especially glass with more permeable and larger cracks. Therefore, the over-expansion might be ascribed to the micro-cracking accumulation arising from overmuch incorporated WGP.

Generally, chemical activation showed a negative effect on ASR expansion when WGP content was low, especially the 10% replacement ratio. However, the positive effect of chemical activation can be observed for samples with 30% WGP (300 μm or 75 μm). In this case, the combination of 2% alkali and 4% sodium sulfate was the optimal choice. It reduced the expansion to 0.086% and 0.046%, respectively, for 300 μm and 75 μm WGP mortar samples. Besides, no apparent regularity was observed between the ASR expansion and the dosage of the chemical agent. However, it can be deduced that the overmuch alkali or sodium sulfate would result in a relatively larger expansion. In contrast, appropriate contents of chemical agents could mitigate the expansion when WGP content is 30%. This could be attributed to the increased concentration of Ca^{2+} and silica reactivity, which reduced the gel swelling potential [40,68]. However, this is indistinct and further investigation needs to be conducted. The AI-based technology was utilised to tackle the relationship between ASR expansion and dosages of the chemical agents, which was specifically described in the following sections.

Similar to the UCS test, the hydrothermal activation was supplemented to compare with chemical and combined activation for 75 μm WGP mortar. The chemical agents' dosage was 2% of alkali and 2% of sodium sulfate. The ASR test results are shown in Fig. 14. The hydrothermal activation was the most effective method in mitigating the ASR expansion for specimens with all WGP replacement ratios. The combined activation could neutralise the effects of chemical and hydrothermal activations so that the ASR expansion was between them. As mentioned before, the pozzolanic reaction of WGP was prone to generate less swelling gels [15]. Therefore, one possible reason for hydrothermal activation effectiveness is the pozzolanic reactivity excitation. However, this still needs further investigation.

4.3. SEM results

SEM analysis presented the smooth surface of 75 μm WGP (N/A), as shown in Fig. 15a. The erosion can be intuitively

(a)
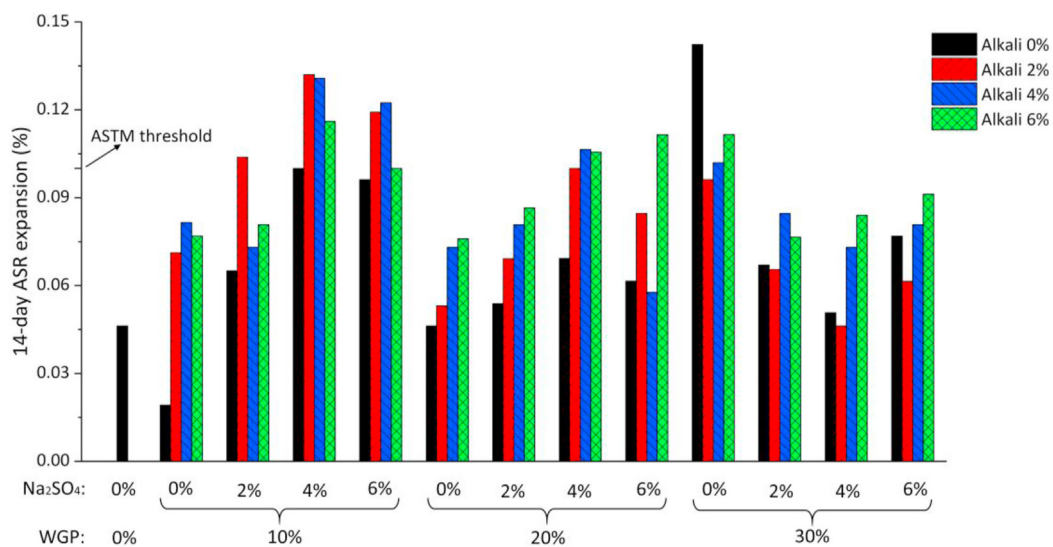
(b)

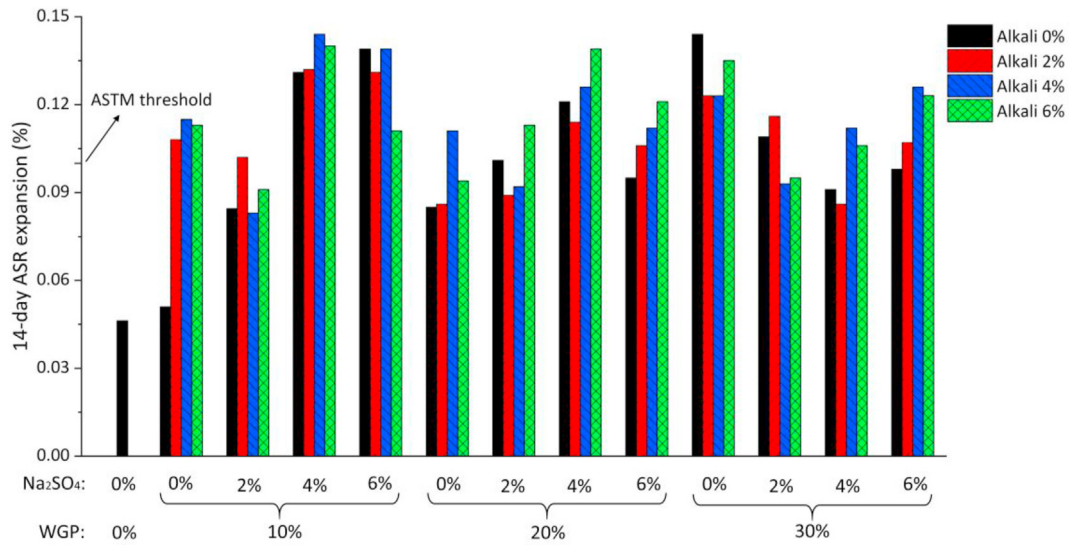**Fig. 13 — ASR expansion for bar specimens containing (a) 300 μm WGP (b) 75 μm WGP at different dosages of sodium sulfate and alkali.**

observed on chemically activated WGP surface with the formation of numerous flocculent deposits (Fig. 15b). This phenomenon ($N-C-S-H$ gels formation) verifies the erosion effect of alkali on glass particles. After hydrothermal activation (Fig. 15c), plenty of tiny glass fragments was observed and the glass edges turned to be blunt, indicating the WGP structural destruction. Fig. 15d depicts the combined-activated WGP, the reaction was the most intense among all the activation approaches. Substantial sediments and a thick gel membrane were generated on the glass surface. Compared to the chemical activation, the combined method possesses higher erosion velocity on the surface of WGP.

This also explains the finding that the highest UCS appeared in combined-activated WGP mortar at both early and late stages.

Fig. 16 shows the schematic images of the silica tetrahedron structural unit and the effects of versatile activation methods on WGP at the molecular level. The chemical activation can contribute to the silica dissolution and the hydrothermal activation is beneficial to the structural depolymerisation (bond rupture and amorphisation). The combined activation possesses the combined effect so that the gels might be thick around the WGP surface. This could be intuitively seen in the above SEM figures.
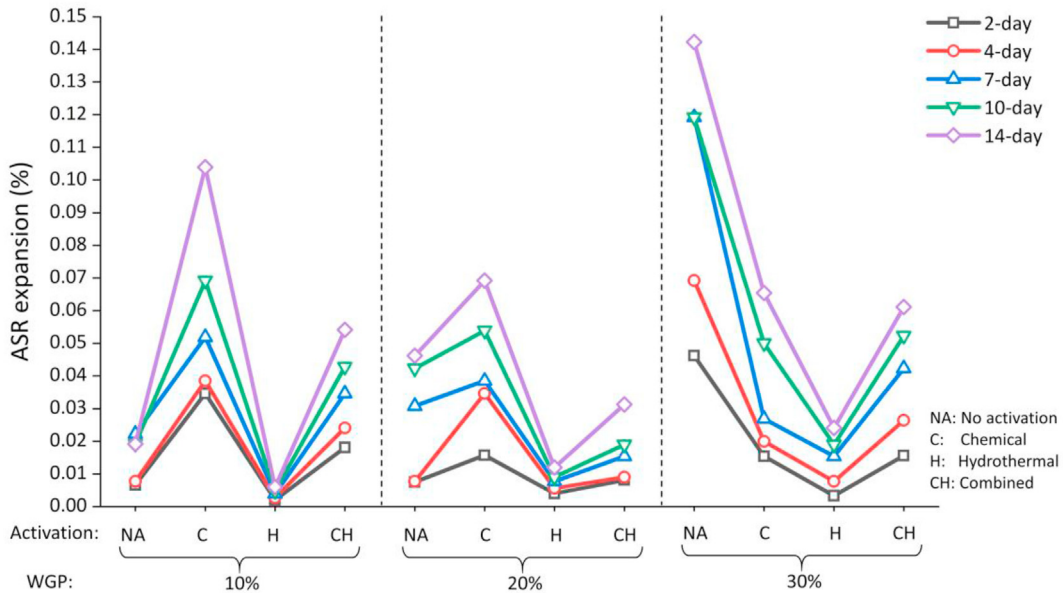
Fig. 14 − **The comparison of ASR expansion of WGP mortar (75 μm) with different activation methods.**

4.4. Results of multi-objective optimisation design

4.4.1. Results of hyperparameter tuning

The ML hyperparameters were tuned through a 10-fold CV and FA algorithm. For instance, the fold possessing the minimum RMSE (UCS dataset: 6th fold, ASR dataset: 3rd fold) during SVR's cross-validation is shown in Fig. 17. Fig. 18 specifically depicts the RMSE iteration on the corresponding folds of different ML models. By comparing the prediction performance of different models in section 4.2.3, the SVR

model was optimal in predicting both UCS and ASR expansion. The corresponding hyperparameters c and γ were 4001.27 and 0.113 for UCS set, and 113.43 and 2.900 for ASR set, respectively.

4.4.2. Performance of FA-SVR

In Fig. 19, the predicted UCS and ASR expansion by employing the optimal ML model (i.e. SVR) were separately compared with the actual values. Most points in training and test sets are close to the perfect fitting curve (the solid diagonal line) so that

(a) WGP-N/A

(b) WGP-chemical activation

(c) WGP-hydrothermal activation

(d) WGP-combined activation
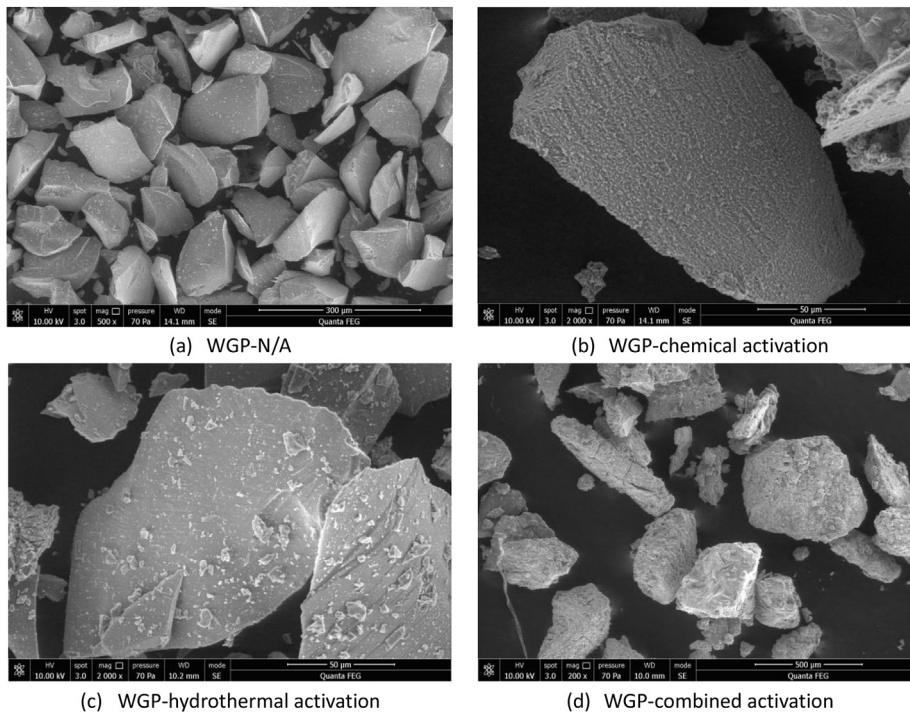
Fig. 15 − **SEM micrographs of WGP under (a) N/A (b) chemical activation (c) hydrothermal activation (d) combined activation.**
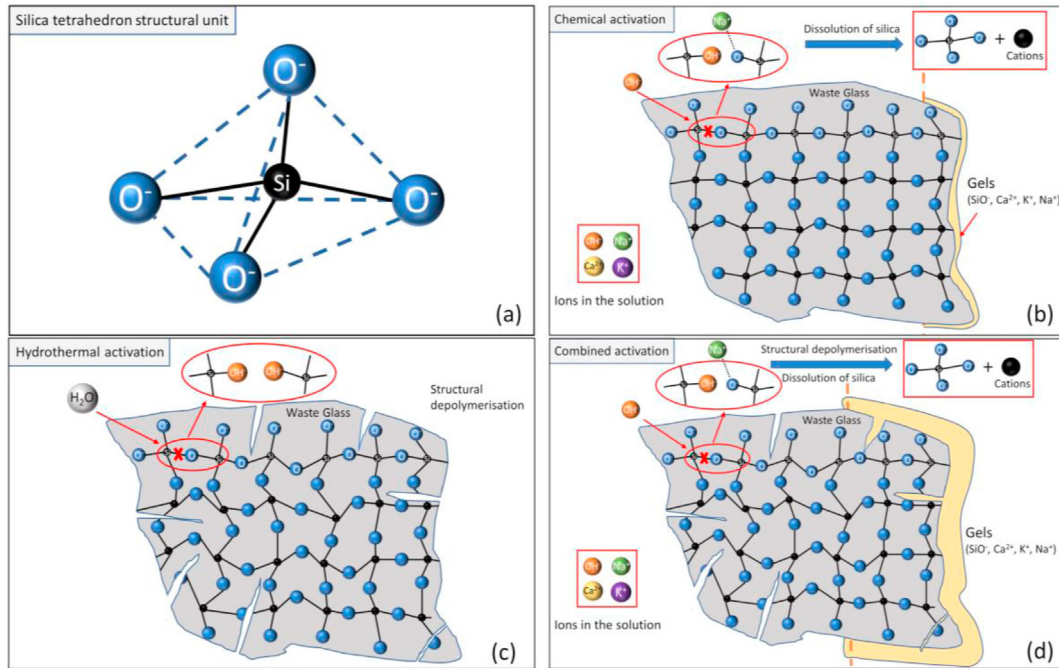
Fig. 16 − Schematic figure of (a) silica tetrahedron structural unit (b) chemical activation (c) hydrothermal activation (d) combined activation.

(a)   (b)
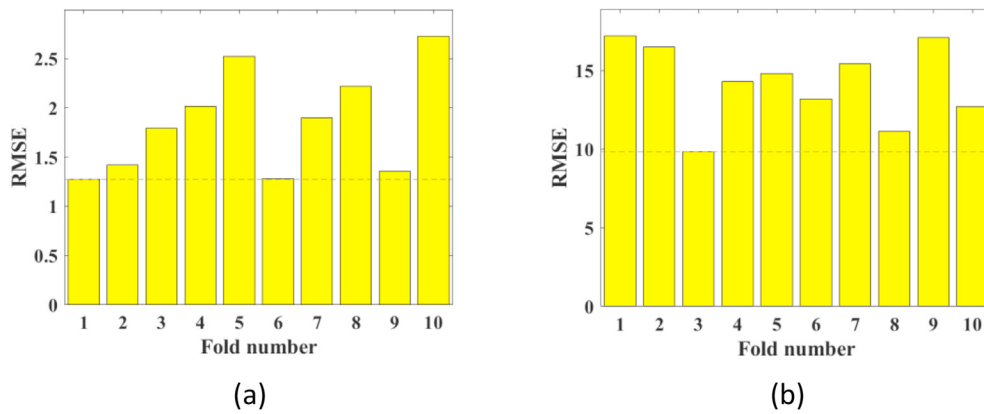
Fig. 17 − 10-fold CV of SVR modelling on the (a) UCS dataset (b) ASR dataset.

(a)   (b)
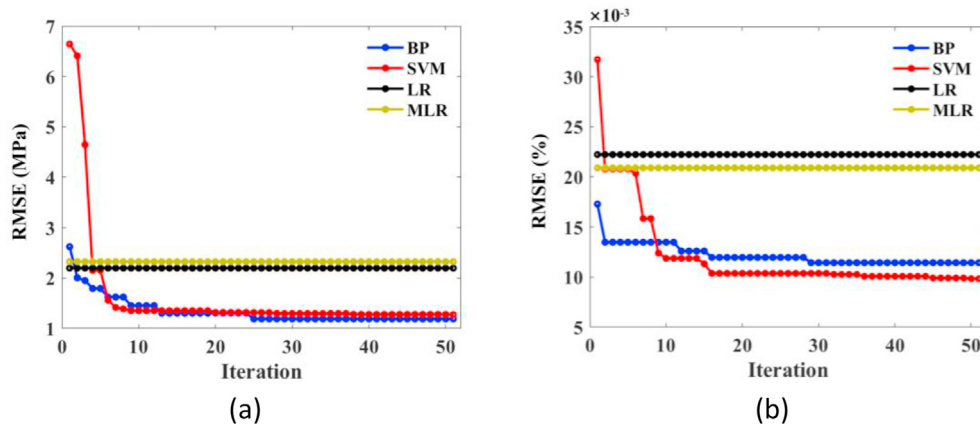
Fig. 18 − RMSE versus iteration in the optimal fold of varying ML models for (a) UCS dataset (b) ASR dataset.
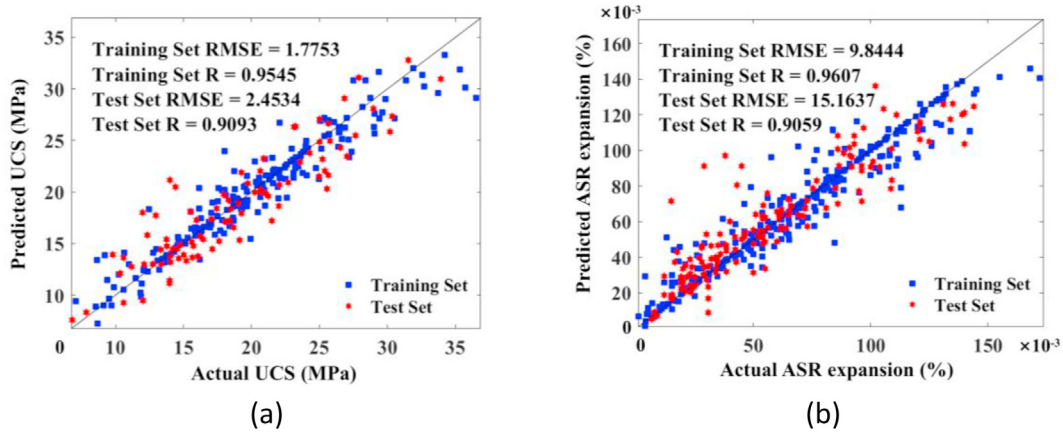
Fig. 19 – Actual versus predicted values for (a) UCS and (b) ASR expansion.

the model prediction ability is relatively robust. This can be further verified by the high values of correlation coefficient (R value), reaching 0.9093 and 0.9059 in the UCS and ASR test sets, respectively. Meanwhile, the RMSE (or R value) on the training and test sets were both similar, which means that the overfitting or under-fitting problem did not exist. Therefore, the established SVR model is feasible to predict the properties of WGP mortar and act as the objective function for the MOO issue.

4.4.3. Model evaluation comparison

Through the box and Taylor diagrams, Fig. 20 intuitively shows the preciseness comparison between SVR, BPNN, LR, and MLR. In the boxplot, the error between the predicted and actual values is plotted shown in Fig. 20 (a) and (b). The SVR model possessed a lower median error (the red line) and a more condensed interquartile range (the space inside the blue rectangle). This phenomenon indicated a lower prediction error than the other ML models. Generally, the SVR model was
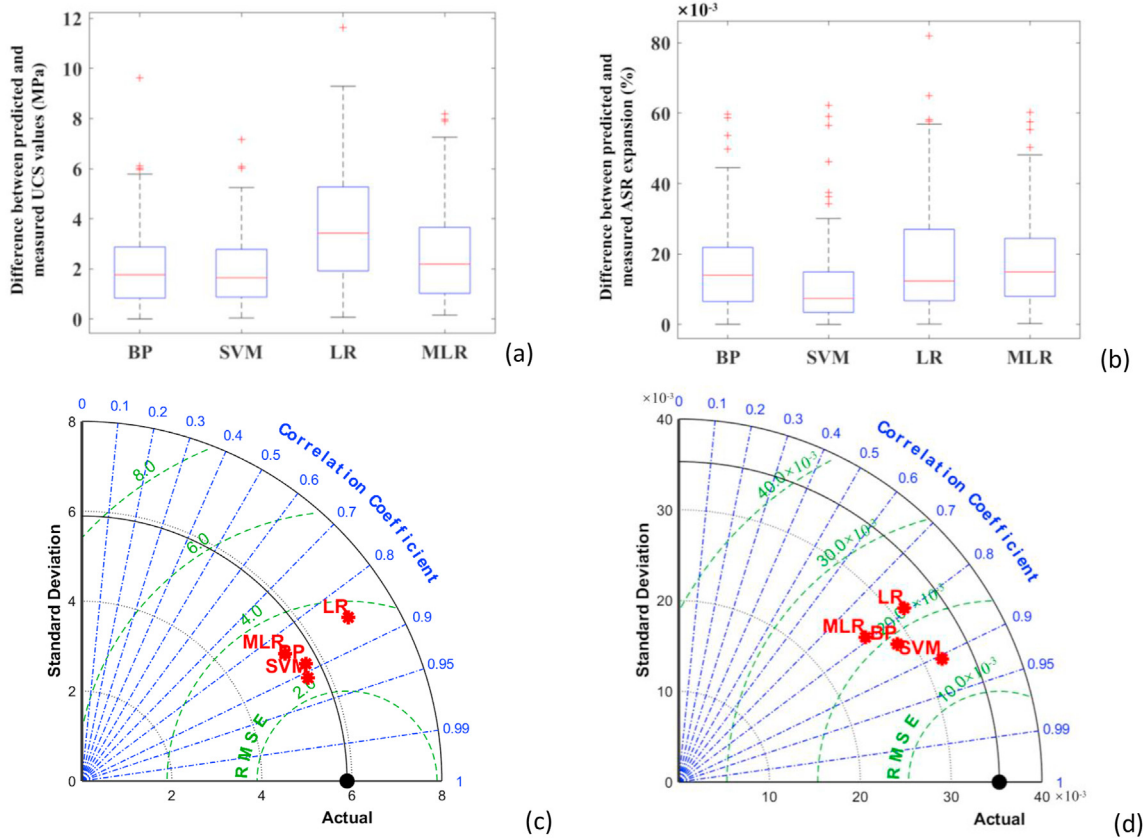
Fig. 20 – Performance evaluation of varying ML models (a) Boxplot of UCS modelling (b) Boxplot of ASR modelling (c) Taylor diagram of UCS modelling (d) Taylor diagram of ASR modelling.

Table 7 − Evaluation of ML models on UCS and ASR test sets.

ML model	Evaluation index			
	RMSE	R	MAE	MAPE
UCS dataset				
BPNN	2.764 MPa	0.885	2.156 MPa	0.129
SVR	2.453 MPa	0.909	1.947 MPa	0.113
LR	4.305 MPa	0.852	3.614 MPa	0.205
MLR	3.137 MPa	0.847	2.549 MPa	0.153
ASR dataset				
BPNN	0.0194%	0.846	0.0154%	0.4764
SVR	0.0152%	0.906	0.0105%	0.2659
LR	0.0242%	0.791	0.0181%	0.3644
MLR	0.0221%	0.790	0.0179%	0.5171
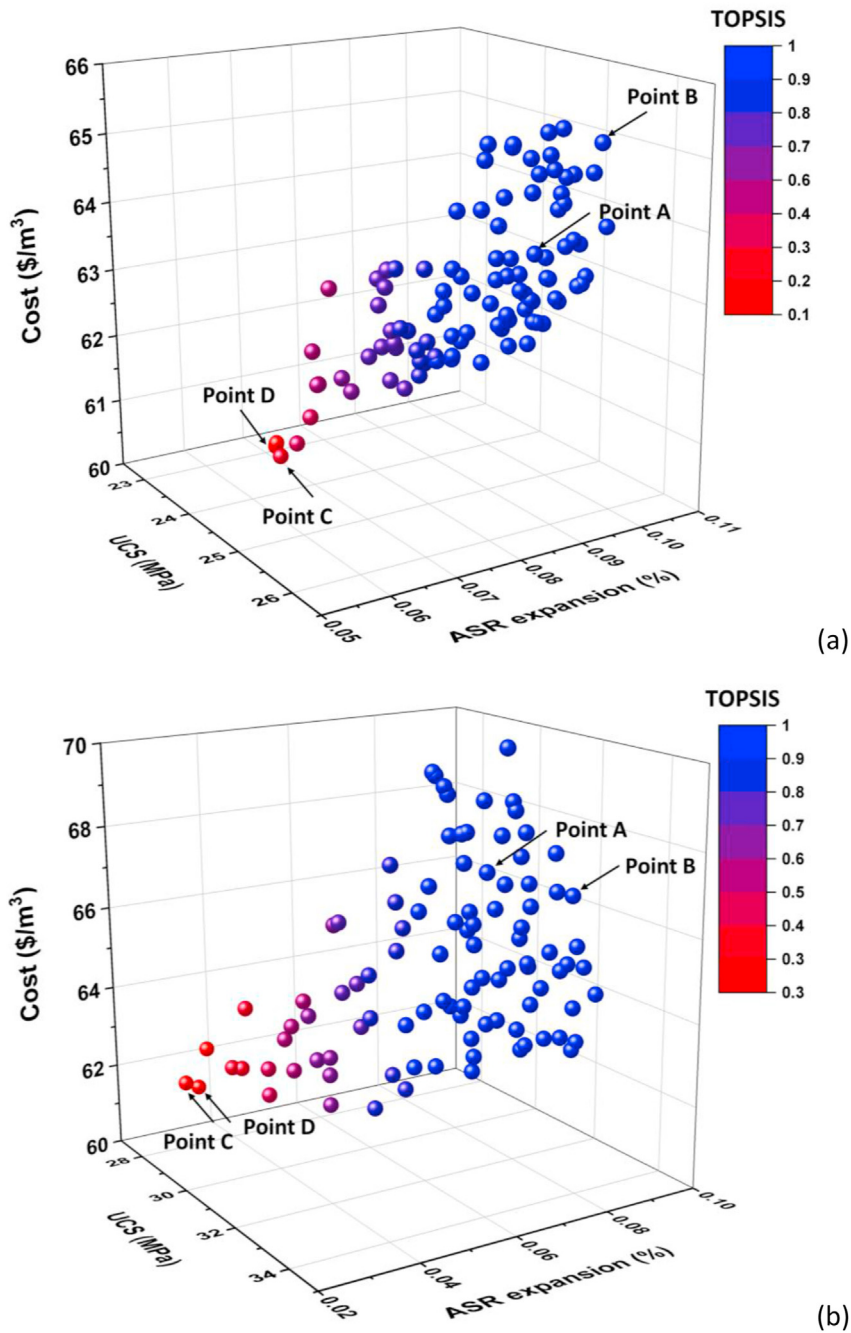
Fig. 21 − Pareto front on cost, UCS, and ASR expansion of (a) 300 μm WGP mortar (b) 75 μm WGP mortar.

Table 8 – Mixture proportions of Pareto solutions of 300 μm WGP mortar.

Mixture	A (Final point)	B	C	D
Cement (kg/m^3)	450	450	450	450
Sand (kg/m^3)	891.64	880.40	953.57	957.62
Water (kg/m^3)	211.5	211.5	211.5	211.5
WGP (kg/m^3)	109.3356	118.19	106.30	107.42
WGP size (μm)	300	300	300	300
Na$_2$SO$_4$ (kg/m^3)	10.70188	12.33	2.87	1.32
Alkali (kg/m^3)	1.31	1.96	0.03	0.65
28-day UCS (MPa)	26.05361	26.13	24.38	23.94
14-day ASR (%)	0.0864	0.0962	0.0617	0.0644
Cost ($/m^3)	63.91	65.29	60.80	60.68
TOPSIS score	1	0.979	0.249	0.112

Table 9 – Mixture proportions of Pareto solutions of 75 μm WGP mortar.

Mixture	A (Final point)	B	C	D
Cement (kg/m^3)	450	450	450	450
Sand (kg/m^3)	882.33	885.52	928.48	930.00
Water (kg/m^3)	211.5	211.5	211.5	211.5
WGP (kg/m^3)	150.97	134.55	112.42	108.35
WGP size (μm)	75	75	75	75
Na$_2$SO$_4$ (kg/m^3)	10.66	13.51	1.58	1.51
Alkali (kg/m^3)	2.94	3.64	0.21	1.04
28-day UCS (MPa)	33.34	33.84	27.73	27.73
14-day ASR (%)	0.0646	0.0796	0.0313	0.0341
Cost ($/m^3)	67.72	67.06	61.53	61.35
TOPSIS score	1	0.967	0.266	0.256

optimal among these ML models although several outliners were produced. Besides, three indices (RMSE, R value, and standard deviation) are integrated into the polar coordinates, as presented in Fig. 20 (c) and (d). Both SVR models were in the closest position to the "actual" points, showing the highest R value, minimum RMSE, and lowest standard deviation among

the four ML models. Furthermore, Table 7 summarises the values of four evaluation indices. The SVR model also possessed the lowest MAE and MAPE indicating its best prediction accuracy. In conclusion, the SVR model is the most suitable to predict the UCS and ASR values of WGP modified mortar.

4.4.4. MOO design

The design solutions that optimised the afore-mentioned tri-objective function were completed by using MOFA-SVR within the constraints. The 100 non-dominated Pareto points were generated showing the combination of UCS, ASR expansion, and cost of 300 μm and 75 μm WGP mortars in Fig. 21a and (b), respectively. The wide distribution of these points in the 3D space with reasonable ranges indicates the effectiveness and generalisation of the established MOBAS-SVR program. For both MOO outcomes of 300 μm and 75 μm WGP mortars, the increase of UCS can only be achieved by cost addition. However, this inevitably increased the risk of damage caused by increased ASR expansion. Therefore, the balance between these three objectives (UCS, ASR expansion, and cost) must be achieved according to the judgement of the decision-maker. Four particular Pareto points (A, B, C, and D) are emphasized in Fig. 21 which corresponds to the highest TOPSIS score, maximum UCS, minimum ASR expansion, and lowest cost, respectively. The specific mixture design of solutions A, B, C, and D are listed in Table 8 and Table 9. Within these Pareto points, Point A was recommended as the preferable and more appropriate solution according to the TOPSIS theory.

4.4.5. Variable sensitivity analysis

The sensitivity of the input variables on the UCS and ASR expansion is quantified in percentage terms depicted in Fig. 22. The curing time is undoubtedly the most significant factor, especially for ASR expansion. The alkali content shows almost the same important degree as curing time for UCS, whereas it insignificantly influences the ASR expansion.
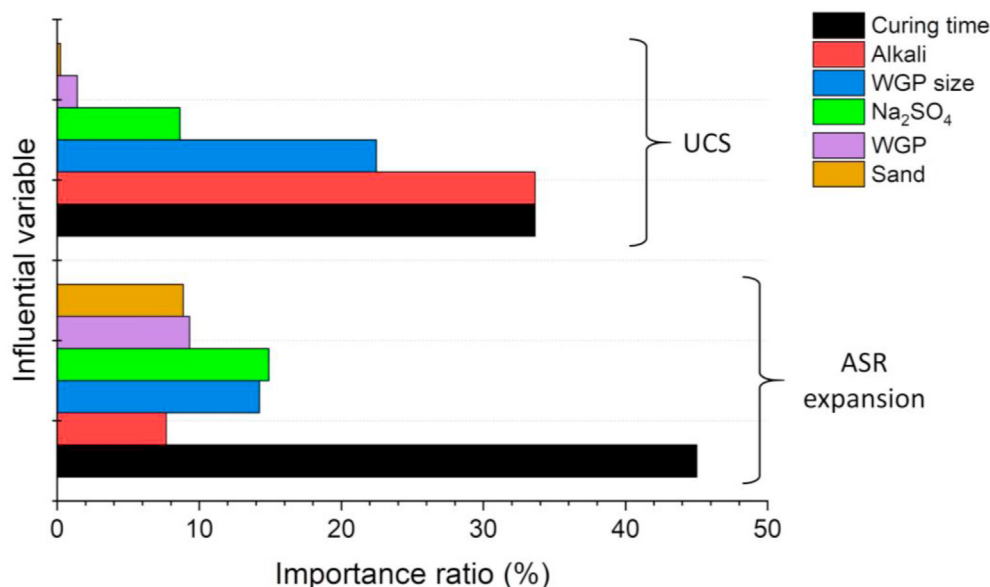

Fig. 22 – Variable significance on UCS and ASR expansion of WGP mortar.

Besides, the WGP size remarkably affects both the ASR expansion and UCS. Compared to the content of Na_2SO_4, the alkali content presents greater influence on UCS and less influence on ASR expansion. These phenomena agree well with the conclusions drawn from the experimental results. In general, the variable's sensitivity analysis provides a quantitative understanding of the variable importance.

5.   Conclusion

In this study, UCS, ASR expansion, and SEM were conducted to investigate WGP mortar and four reactivity excitation methods: mechanical, chemical, hydrothermal, and combined activations. The main conclusions can be drawn and applied to other glass with similar chemical components:

1. Mechanical grinding of WGP from 300 μm to 75 μm effectively enhanced the UCS and reduced the ASR expansion. However, the ASR expansion was still excessive even if 30% WGP (75 μm) was incorporated into the mortar.
2. Alkali and sodium sulfate are two commonly used chemical activators. Regarding UCS improvement, the thresholds of sodium sulfate and alkali are around 2% and 0%–2%, respectively. As to ASR expansion, the chemical activation showed an adequate mitigation effect when the WGP replacement ratio is 30%. The SEM figure showed intuitive alkali erosion on the WGP surface.
3. The hydrothermal activation improved UCS at a late age (28 days) and simultaneously it was the most effective method on reducing ASR expansion. The SEM figure presented numerous tiny broken glass fragments. Besides, the combined activation possessed the optimal effect of strength improvement.
4. The ML (BPNN, SVR, LR, MLR) models were trained with hyperparameters tuned by FA. The SVR showed the best

prediction accuracy and generalisation ability among the four ML models. The corresponding R/RMSE values are 0.909/2.453 MPa and 0.906/0.0152%, respectively on UCS and ASR datasets.
5. By applying MOFA, the Pareto fronts based on three objectives (UCS, ASR, and Cost) were successfully established, guiding the design of both 300 μm and 75 μm WGP mortars. The TOPSIS theory was utilised for decision-making.
6. The sensitivity analysis showed the importance ranking of versatile variables. The alkali is crucial to UCS and the WGP size is essential for both UCS and ASR expansion.

Declaration of Competing Interest

The authors declare that they have no known competing financial interests or personal relationships that could have appeared to influence the work reported in this paper.

Acknowledgements

Appendix

ID	OPC (kg/m³)	75 μm WGP (kg/m³)	300 μm WGP (kg/m³)	Ground silica sand (kg/m³)	Water (kg/m³)	Na₂SO₄ (kg/m³)	Alkali (kg/m³)	Hydro-thermal activation	Compressive strength (MPa)			ASR expansion (%)				
									7d	14d	28d	2d	4d	7d	10d	14d
1	450	0	0	1012.5	211.5	0	0	–	17.44	24.15	26.84	0.0196	0.0225	0.0308	0.0346	0.0462
2	450	101.25	0	911.25	211.5	0	0	–	19.64	27.14	35.72	0.0066	0.0077	0.0156	0.0192	0.0192
3	450	101.25	0	911.25	211.5	0	9	–	17.50	23.06	25.00	0.0500	0.0562	0.0654	0.0692	0.0712
4	450	101.25	0	911.25	211.5	0	18	–	15.02	21.00	23.11	0.0281	0.0385	0.0550	0.0677	0.0815
5	450	101.25	0	911.25	211.5	0	27	–	9.71	12.75	14.49	0.0246	0.0262	0.0308	0.0423	0.0769
6	450	101.25	0	911.25	211.5	9	0	–	19.67	27.01	29.35	0.0009	0.0100	0.0120	0.0350	0.0650
7	450	101.25	0	911.25	211.5	9	9	–	20.89	25.37	29.84	0.0346	0.0385	0.0519	0.0692	0.1038
8	450	101.25	0	911.25	211.5	9	18	–	15.83	20.32	23.63	0.0154	0.0214	0.0315	0.0577	0.0731
9	450	101.25	0	911.25	211.5	9	27	–	13.97	17.63	21.50	0.0246	0.0308	0.0446	0.0538	0.0808
10	450	101.25	0	911.25	211.5	18	0	–	21.92	27.65	36.53	0.0308	0.0369	0.0531	0.0885	0.1000
11	450	101.25	0	911.25	211.5	18	9	–	21.24	26.54	30.34	0.0231	0.0292	0.0538	0.0984	0.1320
12	450	101.25	0	911.25	211.5	18	18	–	16.02	19.45	22.89	0.0154	0.0254	0.0538	0.0808	0.1308
13	450	101.25	0	911.25	211.5	18	27	–	13.98	0.00	18.64	0.0100	0.0231	0.0615	0.0885	0.1160
14	450	101.25	0	911.25	211.5	27	0	–	16.52	21.60	23.61	0.0123	0.0231	0.0654	0.0731	0.0962
15	450	101.25	0	911.25	211.5	27	9	–	16.97	20.42	23.57	0.0038	0.0115	0.0462	0.0846	0.1192
16	450	101.25	0	911.25	211.5	27	18	–	12.78	17.04	19.66	0.0085	0.0231	0.0615	0.1077	0.1224
17	450	101.25	0	911.25	211.5	27	27	–	10.62	14.35	16.33	0.0046	0.0247	0.0462	0.0810	0.1000
18	450	202.5	0	810	211.5	0	0	–	18.13	26.44	27.90	0.0075	0.0138	0.0308	0.0423	0.0462
19	450	202.5	0	810	211.5	0	9	–	18.96	25.77	28.73	0.0192	0.0238	0.0423	0.0462	0.0531
20	450	202.5	0	810	211.5	0	18	–	15.58	20.57	23.97	0.0235	0.0269	0.0423	0.0538	0.0731
21	450	202.5	0	810	211.5	0	27	–	12.37	16.35	18.46	0.0235	0.0269	0.0308	0.0465	0.0760
22	450	202.5	0	810	211.5	9	0	–	22.49	28.96	31.53	0.0308	0.0308	0.0538	0.0515	0.0538
23	450	202.5	0	810	211.5	9	9	–	23.74	30.53	33.92	0.0157	0.0346	0.0385	0.0538	0.0692

— (continued)

ID	OPC (kg/m³)	75 μm WGP (kg/m³)	300 μm WGP (kg/m³)	Ground silica sand (kg/m³)	Water (kg/m³)	Na₂SO₄ (kg/m³)	Alkali (kg/m³)	Hydro-thermal activation	Compressive strength (MPa)			ASR expansion (%)				
									7d	14d	28d	2d	4d	7d	10d	14d
24	450	202.5	0	810	211.5	9	18	−	19.21	21.55	23.12	0.0200	0.0386	0.0465	0.0612	0.0808
25	450	202.5	0	810	211.5	9	27	−	16.08	20.46	25.55	0.0538	0.0577	0.0713	0.0831	0.0865
26	450	202.5	0	810	211.5	18	0	−	21.79	25.66	27.48	0.0346	0.0538	0.0654	0.0692	0.0692
27	450	202.5	0	810	211.5	18	9	−	24.96	29.01	33.73	0.0346	0.0538	0.0615	0.0756	0.1000
28	450	202.5	0	810	211.5	18	18	−	19.25	23.29	25.72	0.0385	0.0615	0.0885	0.1038	0.1065
29	450	202.5	0	810	211.5	18	27	−	9.23	11.99	16.15	0.0421	0.0731	0.0885	0.1077	0.1055
30	450	202.5	0	810	211.5	18	0	−	19.26	25.56	28.40	0.0038	0.0269	0.0423	0.0542	0.0615
31	450	202.5	0	810	211.5	27	9	−	19.70	27.17	30.19	0.0077	0.0192	0.0500	0.0650	0.0846
32	450	202.5	0	810	211.5	27	18	−	17.04	22.70	25.22	0.0154	0.0260	0.0423	0.0462	0.0577
33	450	202.5	0	810	211.5	27	27	−	13.09	18.69	22.60	0.0385	0.0846	0.0962	0.1000	0.1115
34	450	303.75	0	708.75	211.5	0	0	−	17.82	26.44	31.88	0.0462	0.0692	0.1086	0.1192	0.1423
35	450	303.75	0	708.75	211.5	0	9	−	19.59	26.89	31.35	0.0708	0.0731	0.0538	0.0615	0.0962
36	450	303.75	0	708.75	211.5	0	18	−	18.20	23.54	26.05	0.0654	0.0662	0.0727	0.0754	0.1019
37	450	303.75	0	708.75	211.5	0	27	−	14.53	18.93	21.32	0.0769	0.0769	0.0846	0.0769	0.1115
38	450	303.75	0	708.75	211.5	9	0	−	23.45	28.16	34.19	0.0200	0.0250	0.0390	0.0640	0.0670
39	450	303.75	0	708.75	211.5	9	9	−	24.73	29.65	35.33	0.0154	0.0200	0.0269	0.0500	0.0654
40	450	303.75	0	708.75	211.5	9	18	−	18.65	22.95	29.05	0.0165	0.0187	0.0568	0.0765	0.0846
41	450	303.75	0	708.75	211.5	9	27	−	13.78	17.54	21.75	0.0175	0.0254	0.0358	0.0586	0.0765
42	450	303.75	0	708.75	211.5	18	0	−	20.65	25.37	32.57	0.0154	0.0154	0.0238	0.0385	0.0508
43	450	303.75	0	708.75	211.5	18	9	−	22.03	25.65	32.69	0.0192	0.0288	0.0346	0.0427	0.0462
44	450	303.75	0	708.75	211.5	18	18	−	18.80	20.89	23.24	0.0346	0.0538	0.0577	0.0615	0.0731
45	450	303.75	0	708.75	211.5	18	27	−	10.65	12.45	14.01	0.0216	0.0386	0.0462	0.0650	0.0840
46	450	303.75	0	708.75	211.5	27	0	−	18.65	24.06	29.41	0.0154	0.0308	0.0423	0.0654	0.0769
47	450	303.75	0	708.75	211.5	27	9	−	17.96	18.02	22.06	0.0208	0.0269	0.0346	0.0513	0.0615
48	450	303.75	0	708.75	211.5	27	18	−	15.96	22.16	23.82	0.0154	0.0346	0.0486	0.0692	0.0808
49	450	303.75	0	708.75	211.5	27	27	−	13.56	17.06	20.24	0.0268	0.0346	0.0540	0.0654	0.0912
50	450	0	101.25	911.25	211.5	0	0	−	16.20	22.51	25.01	0.0070	0.0150	0.0330	0.0410	0.0510
51	450	0	101.25	911.25	211.5	0	9	−	13.75	18.01	20.23	0.0160	0.0810	0.1090	0.1110	0.1080
52	450	0	101.25	911.25	211.5	0	18	−	12.05	16.80	18.65	0.0490	0.0610	0.0840	0.0950	0.1150
53	450	0	101.25	911.25	211.5	0	27	−	7.86	10.23	11.02	0.0380	0.0450	0.0620	0.0840	0.1130
54	450	0	101.25	911.25	211.5	9	0	−	15.54	21.02	25.04	0.0050	0.0120	0.0230	0.0560	0.0845
55	450	0	101.25	911.25	211.5	9	9	−	18.29	25.40	26.66	0.0270	0.0460	0.0570	0.0950	0.1020
56	450	0	101.25	911.25	211.5	9	18	−	13.77	19.31	20.79	0.0160	0.0250	0.0370	0.0660	0.0830
57	450	0	101.25	911.25	211.5	9	27	−	12.02	16.22	19.13	0.0250	0.0340	0.0620	0.0580	0.0910
58	450	0	101.25	911.25	211.5	18	0	−	17.86	21.65	29.03	0.0490	0.0510	0.0770	0.1200	0.1310
59	450	0	101.25	911.25	211.5	18	9	−	18.69	24.95	26.40	0.0270	0.0340	0.0660	0.1110	0.1320
60	450	0	101.25	911.25	211.5	18	18	−	13.46	19.26	20.83	0.0180	0.0280	0.0720	0.1090	0.1440
61	450	0	101.25	911.25	211.5	18	27	−	12.02	14.65	16.03	0.0110	0.0260	0.0760	0.0960	0.1400
62	450	0	101.25	911.25	211.5	27	0	−	13.00	19.02	18.73	0.0120	0.0540	0.0860	0.1200	0.1390
63	450	0	101.25	911.25	211.5	27	9	−	14.26	19.60	21.45	0.0040	0.0150	0.0520	0.0940	0.1310
64	450	0	101.25	911.25	211.5	27	18	−	10.35	16.19	17.14	0.0090	0.0300	0.0710	0.1340	0.1390
65	450	0	101.25	911.25	211.5	27	27	−	9.13	13.35	14.62	0.0050	0.0350	0.0630	0.0930	0.1110
66	450	0	202.5	810	211.5	0	0	−	15.08	20.94	23.27	0.0210	0.0340	0.0620	0.0700	0.0850
67	450	0	202.5	810	211.5	0	9	−	14.65	21.02	23.22	0.0210	0.0360	0.0540	0.0700	0.0860
68	450	0	202.5	810	211.5	0	18	−	12.11	16.85	19.25	0.0180	0.0640	0.0760	0.0840	0.1110
69	450	0	202.5	810	211.5	0	27	−	9.53	13.56	14.13	0.0300	0.0510	0.0560	0.0730	0.0940
70	450	0	202.5	810	211.5	9	0	−	18.40	22.05	25.65	0.0340	0.0490	0.0720	0.0790	0.1010
71	450	0	202.5	810	211.5	9	9	−	18.36	22.05	25.12	0.0290	0.0380	0.0550	0.0790	0.0890
72	450	0	202.5	810	211.5	9	18	−	14.02	15.52	17.57	0.0210	0.0500	0.0560	0.0800	0.0920
73	450	0	202.5	810	211.5	9	27	−	11.90	13.71	19.93	0.0590	0.0650	0.0820	0.1080	0.1130
74	450	0	202.5	810	211.5	18	0	−	17.02	21.05	24.02	0.0210	0.0650	0.0850	0.1080	0.1210
75	450	0	202.5	810	211.5	18	9	−	17.72	19.73	24.28	0.0440	0.0600	0.0670	0.0920	0.1140
76	450	0	202.5	810	211.5	18	18	−	15.21	17.47	18.78	0.0490	0.0770	0.1040	0.1340	0.1260
77	450	0	202.5	810	211.5	18	27	−	7.07	8.64	12.34	0.0520	0.0850	0.1220	0.1370	0.1390
78	450	0	202.5	810	211.5	27	0	−	15.62	20.65	22.45	0.0069	0.0550	0.0680	0.0760	0.0950
79	450	0	202.5	810	211.5	27	9	−	14.78	19.29	23.09	0.0080	0.0210	0.0550	0.0810	0.1060
80	450	0	202.5	810	211.5	27	18	−	13.22	15.89	18.30	0.0170	0.0280	0.0490	0.0840	0.1120
81	450	0	202.5	810	211.5	27	27	−	10.60	13.83	17.29	0.0420	0.1130	0.1250	0.1290	0.1210
82	450	0	303.75	708.75	211.5	0	0	−	14.36	19.03	21.69	0.0410	0.0760	0.0860	0.1300	0.1440
83	450	0	303.75	708.75	211.5	0	9	−	15.12	21.98	25.65	0.0420	0.0650	0.0810	0.0960	0.1230
84	450	0	303.75	708.75	211.5	0	18	−	14.05	18.05	22.01	0.0800	0.1050	0.1210	0.1280	0.1230
85	450	0	303.75	708.75	211.5	0	27	−	11.85	15.65	17.12	0.1020	0.1260	0.1160	0.1210	0.1350
86	450	0	303.75	708.75	211.5	9	0	−	18.00	22.05	27.35	0.0760	0.0790	0.0870	0.0910	0.1090
87	450	0	303.75	708.75	211.5	9	9	−	15.33	20.65	22.61	0.0390	0.0530	0.0860	0.1130	0.1160
88	450	0	303.75	708.75	211.5	9	18	−	11.19	16.98	19.17	0.0130	0.0150	0.0290	0.0560	0.0930
89	450	0	303.75	708.75	211.5	9	27	−	8.54	12.10	13.33	0.0280	0.0370	0.0430	0.0650	0.0950
90	450	0	303.75	708.75	211.5	18	0	−	16.22	20.65	27.02	0.0320	0.0290	0.0400	0.0650	0.0910
91	450	0	303.75	708.75	211.5	18	9	−	14.54	18.47	21.58	0.0320	0.0530	0.0640	0.0710	0.0860

— (continued)

ID	OPC (kg/m³)	75 μm WGP (kg/m³)	300 μm WGP (kg/m³)	Ground silica sand (kg/m³)	Water (kg/m³)	Na₂SO₄ (kg/m³)	Alkali (kg/m³)	Hydro-thermal activation	Compressive strength (MPa)			ASR expansion (%)				
									7d	14d	28d	2d	4d	7d	10d	14d
92	450	0	303.75	708.75	211.5	18	18	—	11.47	15.88	16.15	0.0620	0.0950	0.1040	0.1030	0.1120
93	450	0	303.75	708.75	211.5	18	27	—	6.82	9.39	9.80	0.0370	0.0730	0.0850	0.0890	0.1060
94	450	0	303.75	708.75	211.5	27	0	—	14.21	19.65	24.06	0.0310	0.0480	0.0810	0.0860	0.0980
95	450	0	303.75	708.75	211.5	27	9	—	10.60	12.97	14.41	0.0390	0.0480	0.0600	0.0860	0.1070
96	450	0	303.75	708.75	211.5	27	18	—	9.89	15.73	16.29	0.0260	0.0620	0.0840	0.1220	0.1260
97	450	0	303.75	708.75	211.5	27	27	—	8.68	11.94	13.97	0.0500	0.0600	0.0800	0.0930	0.1231
98	450	101.25	0	911.25	211.5	0	0	√	20.76	27.02	34.02	0.0020	0.0027	0.0039	0.0048	0.0060
99	450	101.25	0	911.25	211.5	9	9	√	21.51	27.2	34.65	0.0181	0.0241	0.0346	0.0428	0.0541
100	450	202.5	0	810	211.5	0	0	√	19.1	28.46	31.97	0.0040	0.0056	0.0077	0.0090	0.0120
101	450	202.5	0	810	211.5	9	9	√	22.06	30.33	34.68	0.0081	0.0090	0.0154	0.0190	0.0313
102	450	303.75	0	708.75	211.5	0	0	√	20.15	27.65	35.13	0.0033	0.0077	0.0154	0.0190	0.0241
103	450	303.75	0	708.75	211.5	9	9	√	24.71	30.11	36.5	0.0156	0.0264	0.0423	0.0523	0.0611

REFERENCES

[1] Tang Y, Feng W, Chen Z, Nong Y, Guan S, Sun J. Fracture behavior of a sustainable material: recycled concrete with waste crumb rubber subjected to elevated temperatures. J Clean Prod 2021:128553.

[2] Li J, Qin Q, Sun J, Ma Y, Li Q. Mechanical and conductive performance of electrically conductive cementitious composite using graphite, steel slag, and GGBS. Structural Concrete; 2020.

[3] Aslani F, Sun J, Huang G. Mechanical behavior of fiber-reinforced self-compacting rubberized concrete exposed to elevated temperatures. J Mater Civ Eng 2019;31(12):04019302.

[4] Aslani F, Sun J, Bromley D, Ma G. Fiber-reinforced lightweight self-compacting concrete incorporating scoria aggregates at elevated temperatures. Struct Concr 2019;20(3):1022—35.

[5] Aslani F, Hou L, Nejadi S, Sun J, Abbasi S. Experimental analysis of fiber-reinforced recycled aggregate self-compacting concrete using waste recycled concrete aggregates, polypropylene, and steel fibers. Struct Concr 2019;20(5):1670—83.

[6] Gin S, Abdelouas A, Criscenti LJ, Ebert WL, Ferrand K, Geisler T, et al. An international initiative on long-term behavior of high-level nuclear waste glass. Mater Today 2013;16(6):243—8. https://doi.org/10.1016/j.mattod.2013.06.008.

[7] Feng J, Chen B, Sun W, Wang Y. Microbial induced calcium carbonate precipitation study using Bacillus subtilis with application to self-healing concrete preparation and characterization. Construct Build Mater 2021;280:122460. https://doi.org/10.1016/j.conbuildmat.2021.122460.

[8] Wang J, Dai Q, Si R. Experimental and numerical investigation of fracture behaviors of steel fiber—reinforced rubber self-compacting concrete. J Mater Civ Eng 2022;34(1):04021379.

[9] Wang J, Dai Q, Si R, Guo S. Investigation of properties and performances of Polyvinyl Alcohol (PVA) fiber-reinforced rubber concrete. Construct Build Mater 2018;193:631—42.

[10] Mohajerani A, Vajna J, Cheung THH, Kurmus H, Arulrajah A, Horpibulsuk S. Practical recycling applications of crushed waste glass in construction materials: a review. Construct Build Mater 2017;156:443—67. https://doi.org/10.1016/j.conbuildmat.2017.09.005.

[11] Wang J, Dai Q, Si R, Guo S. Mechanical, durability, and microstructural properties of macro synthetic polypropylene (PP) fiber-reinforced rubber concrete. J Clean Prod 2019;234:1351—64.

[12] Wang J, Dai Q, Si R, Ma Y, Guo S. Fresh and mechanical performance and freeze-thaw durability of steel fiber-reinforced rubber self-compacting concrete (SRSCC). J Clean Prod 2020;277:123180.

[13] Shi C, Zheng K. A review on the use of waste glasses in the production of cement and concrete. Resour Conserv Recycl 2007;52(2):234—47.

[14] Wang J, Dai Q, Guo S, Si R. Study on rubberized concrete reinforced with different fibers. ACI Mater J 2019;116(2).

[15] Du H, Tan KH. Use of waste glass as sand in mortar: Part II — alkali—silica reaction and mitigation methods. Cement Concr Compos 2013;35(1):118—26. https://doi.org/10.1016/j.cemconcomp.2012.08.029.

[16] Liu J, Wu C, Wu G, Wang X. A novel differential search algorithm and applications for structure design. Appl Math Comput 2015;268:246—69.

[17] Wang L, Yuan J, Wu C, Wang X. Practical algorithm for stochastic optimal control problem about microbial fermentation in batch culture. Optimization Letters 2019;13(3):527—41.

[18] Lam CS, Poon CS, Chan D. Enhancing the performance of pre-cast concrete blocks by incorporating waste glass—ASR consideration. Cement Concr Compos 2007;29(8):616—25.

[19] Chen FX, Zhong YC, Gao XY, Jin ZQ, Wang ED, Zhu FP, et al. Non-uniform model of relationship between surface strain and rust expansion force of reinforced concrete. Sci Rep 2021;11(1):1—9. https://doi.org/10.21203/rs.3.rs-135397/v1.

[20] Chen F, Jin Z, Wang E, Wang L, Jiang Y, Guo P, et al. Relationship model between surface strain of concrete and expansion force of reinforcement rust. Sci Rep 2021;11(1):1—11. https://doi.org/10.1038/s41598-021-83376-w.

[21] Sun J, Aslani F, Lu J, Wang L, Huang Y, Ma G. Fresh and mechanical behaviour of developed fibre-reinforced lightweight engineered cementitious composites for 3D concrete printing containing hollow glass microspheres. Ceram Int 2021;47(19):27107—21.

[22] Singh V, Gu N, Wang X. A theoretical framework of a BIM-based multi-disciplinary collaboration platform. Autom ConStruct 2011;20(2):134—44.

[23] Al-Buriahi M, Singh V. Comparison of shielding properties of various marble concretes using GEANT4 simulation and experimental data. Journal of the Australian Ceramic Society 2020;56(3):1127—33.

[24] Al-Buriahi MS, Singh VP, Alalawi A, Sriwunkum C, Tonguc BT. Mechanical features and radiation shielding properties of TeO2—Ag2O—WO3 glasses. Ceram Int 2020;46(10):15464—72.

[25] Alzahrani JS, Alothman MA, Eke C, Al-Ghamdi H, Aloraini DA, Al-Buriahi MS. Simulating the radiation shielding properties of TeO2—Na2O—TiO glass system using PHITS Monte Carlo code. Comput Mater Sci 2021;196:110566.

[26] Singh J, Kumar V, Vermani YK, Al-Buriahi MS, Alzahrani JS, Singh T. Fabrication and characterization of barium based

bioactive glasses in terms of physical, structural, mechanical and radiation shielding properties. Ceram Int 2021;47(15):21730–43.

[27] Kebaili I, Znaidia S, Alzahrani JS, Alothman MA, Boukhris I, Olarinoye IO, et al. Ge 20 Se 80-x Bi x (x≤ 12) chalcogenide glasses for infrared and gamma sensing applications: structural, optical and gamma attenuation aspects. J Mater Sci Mater Electron 2021:1–14.

[28] Sun J, Wang X, Zhang J, Xiao F, Sun Y, Ren Z, et al. Multi-objective optimisation of a graphite-slag conductive composite applying a BAS-SVR based model. J Build Eng 2021;44:103223.

[29] Sun J, Ma Y, Li J, Zhang J, Ren Z, Wang X. Machine learning-aided design and prediction of cementitious composites containing graphite and slag powder. J Build Eng 2021:102544.

[30] Zhang W, Li H, Li Y, Liu H, Chen Y, Ding X. Application of deep learning algorithms in geotechnical engineering: a short critical review. Artif Intell Rev 2021;(9):1–41.

[31] Zhang W, Wu C, Zhong H, Li Y, Wang L. Prediction of undrained shear strength using extreme gradient boosting and random forest based on Bayesian optimization. Geosci Front 2021;12(1):469–77.

[32] Sun J, Wang Y, Yao X, Ren Z, Zhang G, Zhang C, et al. Machine-learning-Aided prediction of flexural strength and ASR expansion for waste glass cementitious composite. Appl Sci 2021;11(15):6686.

[33] Zhang R, Wu C, Goh AT, Böhlke T, Zhang W. Estimation of diaphragm wall deflections for deep braced excavation in anisotropic clays using ensemble learning. Geosci Front 2021;12(1):365–73.

[34] Xu S, Wang J, Shou W, Ngo T, Sadick AM, Wang X. Computer vision techniques in construction: a critical review. Arch Comput Methods Eng 2021;28(5):3383–97. https://doi.org/10.1007/s11831-020-09504-3.

[35] Feng W, Wang Y, Sun J, Tang Y, Wu D, Jiang Z, et al. Prediction of thermo-mechanical properties of rubber-modified recycled aggregate concrete. Construct Build Mater 2022;318:125970.

[36] Sun J, Aslani F, Wei J, Wang X. Electromagnetic absorption of copper fiber oriented composite using 3D printing. Construct Build Mater 2021;300:124026.

[37] Zhang J, Sun Y, Li G, Wang Y, Sun J, Li J. Machine-learning-assisted shear strength prediction of reinforced concrete beams with and without stirrups. Eng Comput 2020:1–15.

[38] Zhang W, Zhang R, Wu C, Goh ATC, Lacasse S, Liu Z, et al. State-of-the-art review of soft computing applications in underground excavations. Geosci Front 2020;11(4):1095–106.

[39] Wu C, Wang X, Chen M, Kim MJ. Differential received signal strength based RFID positioning for construction equipment tracking. Adv Eng Inf 2019;42:100960.

[40] Huang H, Huang M, Zhang W, Yang S. Experimental study of predamaged columns strengthened by HPFL and BSP under combined load cases. Structure and infrastructure engineering 2021;17(9):1210–27. https://doi.org/10.1080/15732479.2020.1801768.

[41] Cheng M-Y, Prayogo D, Wu Y-W. Novel genetic algorithm-based evolutionary support vector machine for optimizing high-performance concrete mixture. J Comput Civ Eng 2014;28(4):06014003.

[42] Zhang J, Huang Y, Wang Y, Ma G. Multi-objective optimization of concrete mixture proportions using machine learning and metaheuristic algorithms. Construct Build Mater 2020;253:119208. https://doi.org/10.1016/j.conbuildmat.2020.119208.

[43] ASTM. Standard specification for standard sand. C778-13. 2013.

[44] Standard A. Standard specification for coal fly ash and raw or calcined natural pozzolan for use in concrete. ASTM Standard C; 2012. p. 618.

[45] Xu J, Wu Z, Chen H, Shao L, Zhou X, Wang S. Study on strength behavior of basalt fiber-reinforced loess by digital image technology (DIT) and scanning electron microscope (SEM). Arabian J Sci Eng 2021:1–20. https://doi.org/10.1007/s13369-021-05787-1.

[46] Zhang W, Tang Z, Yang Y, Wei J, Stanislav P. Mixed-mode debonding behavior between CFRP plates and concrete under fatigue loading. J Struct Eng 2021;147(5):04021055. https://doi.org/10.1061/(ASCE)ST.1943-541X.0003032.

[47] Standard A. C305. Standard practice for mechanical mixing of hydraulic cement pastes and mortars of plastic consistency. West Conshohocken, PA: ASTM International; 2014.

[48] Astm C. Standard test method for potential alkali reactivity of aggregates (mortar-bar method). 2007.

[49] Basak D, Pal S, Patranabis DC. Support vector regression. Neural Information Processing-Letters and Reviews 2007;11(10):203–24.

[50] Boyd S, Vandenberghe L. Convex optimization. Cambridge University Press; 2004.

[51] Baykasoğlu A, Öztaş A, Özbay E. Prediction and multi-objective optimization of high-strength concrete parameters via soft computing approaches. Expert Syst Appl 2009;36(3):6145–55.

[52] Zhang WG, Li HR, Wu CZ, Li YQ, Liu ZQ, Liu HL. Soft computing approach for prediction of surface settlement induced by earth pressure balance shield tunneling. Undergr Space 2021;6(4):353–63.

[53] Yoon KP, Hwang C-L. Multiple attribute decision making: an introduction. Sage publications; 1995.

[54] Schwarz N, Cam H, Neithalath N. Influence of a fine glass powder on the durability characteristics of concrete and its comparison to fly ash. Cement Concr Compos 2008;30(6):486–96.

[55] Zhang L, Xu Y, Liu H, Li Y, You S, Zhao J, et al. Effects of coexisting Na+, Mg2+ and Fe3+ on nitrogen and phosphorus removal and sludge properties using A2O process. J Water Proc Eng 2021;44:102368. https://doi.org/10.1016/j.jwpe.2021.102368.

[56] Pascual AB, Tognonvi MT, Tagnit-Hamou A. Waste glass powder-based alkali-activated mortar. Int. J. Res. Eng. Technol 2014;3(13):32–6.

[57] Shi C. Corrosion of glasses and expansion mechanism of concrete containing waste glasses as aggregates. J Mater Civ Eng 2009;21(10):529–34.

[58] Mou B, Bai Y. Experimental investigation on shear behavior of steel beam-to-CFST column connections with irregular panel zone. Eng Struct 2018;168:487–504. https://doi.org/10.1016/j.engstruct.2018.04.029.

[59] Way S, Shayan A. Early hydration of a Portland cement in water and sodium hydroxide solutions: composition of solutions and nature of solid phases. Cement Concr Res 1989;19(5):759–69.

[60] Xu D-s, Huang M, Zhou Y. One-dimensional compression behavior of calcareous sand and marine clay mixtures. Int J GeoMech 2020;20(9):04020137. https://doi.org/10.1061/(ASCE)GM.1943-5622.0001763.

[61] Sun J, Huang Y, Aslani F, Wang X, Ma G. Mechanical enhancement for EMW-absorbing cementitious material using 3D concrete printing. J Build Eng 2021:102763.

[62] Sun J, Lin S, Zhang G, Sun Y, Zhang J, Chen C, et al. The effect of graphite and slag on electrical and mechanical properties of electrically conductive cementitious composites. Construct Build Mater 2021;281:122606.

[63] Du Toit G, Kearsley EP, Mc Donald JM, Kruger RA, van der Merwe EM. Chemical and mechanical activation of hybrid fly ash cement. Adv Cement Res 2018;30(9):399—412. https://doi.org/10.1680/jadcr.17.00156.

[64] Xu D, Liu Q, Qin Y, Chen B. Analytical approach for crack identification of glass fiber reinforced polymer—sea sand concrete composite structures based on strain dissipations. Struct Health Monit 2020. https://doi.org/10.1177/1475921720974290. 1475921720974290.

[65] Sun J, Wang Y, Liu S, Dehghani A, Xiang X, Wei J, et al. Mechanical, chemical and hydrothermal activation for waste glass reinforced cement. Construct Build Mater 2021;301:124361.

[66] Zhang C, Ali A, Sun L. Investigation on low-cost friction-based isolation systems for masonry building structures: experimental and numerical studies, vol. 243. Engineering Structures; 2021. p. 112645. https://doi.org/10.1016/j.engstruct.2021.112645.

[67] Shayan A, Xu A. Value-added utilisation of waste glass in concrete. Cement Concr Res 2004;34(1):81—9.

[68] Beyene M, Snyder A, Lee RJ, Blaszkiewicz M. Alkali Silica Reaction (ASR) as a root cause of distress in a concrete made from Alkali Carbonate Reaction (ACR) potentially susceptible aggregates. Cement Concr Res 2013;51:85—95.